Journal of Scientific Computing manuscript No.
(will be inserted by the editor)

Accurate high-order tensor-product generalized summation-by-parts discretizations of hyperbolic conservation laws: general curved domains and functional superconvergence

David A. Craig Penner · David W. Zingg

Received: date / Accepted: date

Abstract The goal of this paper is to outline the requirements for obtaining accurate solutions and functionals from high-order tensor-product generalized summation-by-parts discretizations of the steady two-dimensional linear convection and Euler equations on general curved domains. Two procedures for constructing high-order grids using either Lagrange or B-spline mappings are outlined. For the linear convection equation, four discretizations are derived and characterized—two based on the mortar-element approach and two based on the global summation-by-parts-operator approach. It is shown numerically that the schemes are dual consistent, and the requirements for achieving functional superconvergence for each set of methods are outlined. For the Euler equations, a dual-consistent mortar-element discretization is proposed and the practical requirements for obtaining accurate solutions and superconvergent functionals for problems of increasing practical relevance are delineated through theory and numerical examples.

Keywords generalized summation-by-parts operators · functional superconvergence · curvilinear coordinates · dual consistency · computational fluid dynamics · high-order methods

Mathematics Subject Classification (2020) 65N06 · 65N12 · 65N50

1 Introduction

This work is concerned with obtaining accurate solutions and, particularly, functionals in the context of high-order computational fluid dynamics simu-

D. A. Craig Penner
University of Toronto Institute for Aerospace Studies, Toronto, Canada
E-mail: david.craigpenner@mail.utoronto.ca

D. W. Zingg
University of Toronto Institute for Aerospace Studies, Toronto, Canada
E-mail: dwz@utias.utoronto.ca

lations. Practically, in the context of aerodynamic shape optimization for example, obtaining accurate functionals is especially important, as the objective function and constraints driving the overall optimization procedure typically depend primarily on functionals like lift and drag and only implicitly depend on the accuracy of the numerical solution through these same functionals (see, for example, [16]). Furthermore, the time it takes to reach a specified error tolerance can be reduced by increasing functional accuracy for a given number of degrees of freedom, which translates to faster flow solution times overall. These factors taken together motivate the present focus on obtaining accurate functionals.

Several authors have investigated sufficient conditions that result in functional superconvergence for a range of numerical schemes. These include Pierce and Giles [27], Lu [22], Hartmann [13], and, more recently, Hartmann and Leicht [14] and Cockburn and Wang [4]. Across many of these approaches, a recurring theme, initially understood in the context of discontinuous Galerkin schemes, is the concept of dual consistency as an enabling property that a given discretization should satisfy to achieve functional superconvergence. Of particular importance for the present work, Hicken and Zingg [17] showed that dual-consistent discretizations of scalar linear hyperbolic and elliptic partial differential equations (PDEs) constructed with classical diagonal-norm summation-by-parts (SBP) operators and simultaneous approximation terms (SATs) achieve functional superconvergence for sufficiently smooth problems. Subsequently, Hicken and Zingg [18] outlined how to construct a dual-consistent classical SBP-SAT discretization of the Euler equations and numerically showed that the dual-consistent scheme outperforms a dual-inconsistent scheme with respect to functional convergence. Around this time, Del Rey Fernández *et al.* [8] introduced a generalization of classical tensor-product SBP operators that extended the SBP approach to a broader class of operators, hereafter referred to as generalized SBP operators. Details of the development of the SBP-SAT approach over the last several decades can be found in the review papers by Del Rey Fernández *et al.* [9] and Svärd and Nordström [29].

Compared to discretizations based on classical SBP (CSBP) operators, sufficient conditions for realizing functional superconvergence with generalized SBP discretizations are not as well understood. In their initial generalization, Del Rey Fernández *et al.* [8] considered a steady one-dimensional linear problem and showed, numerically, that the integral of the solution over the domain superconverged at a rate of approximately $\tau + 1$, where τ is the degree of the quadrature rule associated with a given SBP operator. Subsequently, Boom and Zingg [3] and Boom [2] extended some of the linear results of Hicken and Zingg [17] to time-marching methods constructed with generalized SBP operators. For discretizations based on multidimensional SBP operators, Del Rey Fernández *et al.* [10] found that the energy error for a two-dimensional discretization of the linear convection equation superconverged at rates of $2p$ and $2p + 1$ for the SBP-Γ and SBP-Ω schemes, respectively. Yan *et al.* [34] investigated multidimensional SATs for linear diffusion-type PDEs and found that the volume functional considered converged at a rate of $2p$ for both the

SBP-Γ and SBP-Ω schemes. More recently, Worku and Zingg [33] extended the framework of Yan *et al.* [34] to encompass additional types of SATs and demonstrated that degree p dual consistent multidimensional SBP discretizations of linear diffusion-type PDEs exhibit $2p$ functional superconvergence. For discretizations constructed using tensor-product generalized SBP operators, it was previously shown in Craig Penner and Zingg [5] that for some linear hyperbolic PDEs, Legendre-Gauss-Lobatto (LGL) operators outperform Legendre-Gauss (LG) operators with respect to functional accuracy when the degree of the geometry is greater than the degree of the underlying discretization, the volume metric terms are approximated using the same generalized SBP operator used to discretize the flux terms, and the surface metric terms are constructed by extrapolating the volume metric terms (hereafter referred to as the baseline approach for the metrics).

In the present work, two procedures for constructing high-order grids using Lagrange polynomials and B-splines are outlined. Next, the investigation of functional accuracy in [5] is extended in the following two directions, focusing on element-type tensor-product generalized SBP methods. First, building upon the discretizations developed in Del Rey Fernández *et al.* [7], four tensor-product generalized SBP discretizations of the two-dimensional linear convection equation are considered (two based on the mortar-element approach and two based on the global SBP-operator approach). It is demonstrated numerically that the schemes are dual consistent, and the requirements for achieving functional superconvergence are outlined for each set of schemes. Here, the term functional superconvergence is used to refer to the phenomenon whereby integral functionals based on a degree p discretization converge at a rate of at least $2p$ under uniform refinement, despite the numerical solution only converging at a nominal rate of about $p+1$ for sufficiently smooth problems. Second, using information gained from the analysis of the linear convection equation, a representative mortar-element discretization approximating the divergence form of the two-dimensional Euler equations is presented and sufficient conditions for achieving accurate solutions and functional superconvergence are delineated.

2 Notation

The notation in this paper is similar to that used in [6,7]. Upper-case letters in sans-serif font (e.g., H) and lower-case bold font (e.g., $\boldsymbol{u}$) are used to denote matrices and vectors, respectively, while upper-case letters in script font (e.g., $\mathcal{U}$) and upper-case letters in bold script font (e.g., $\boldsymbol{\mathcal{U}}$) are used to denote scalar- and vector-valued functions, respectively. Let $\Omega \subset \mathbb{R}^2$ denote a two-dimensional domain in Cartesian coordinates $[x_1, x_2] \in \mathbb{R}^2$ having the boundary $\partial\Omega$. For each discretization, the physical domain is decomposed into several nonoverlapping elements, and element-local time-invariant invertible transformations (satisfying, for example, Assumption 1 in [7,25]) are used to express each physical element in terms of the computational domain

$\hat{\Omega} = [\alpha_{\xi_1}, \beta_{\xi_1}] \times [\alpha_{\xi_2}, \beta_{\xi_2}]$ in computational coordinates $[\xi_1, \xi_2] \in \mathbb{R}^2$ having the boundary $\hat{\Gamma}$. The face numbering convention used in this work is identical to that summarized in Table 1 in [7]. Furthermore, occasionally big O notation is used where the term $\mathcal{P}(h)$, for example, is order $p+1$, i.e., $\mathcal{P}(h) = \mathcal{O}(h^{p+1})$, if and only if there exist constants $C > 0$ and $h_\star > 0$ such that

$$|\mathcal{P}(h)| \leq Ch^{p+1} \quad \forall h < h_\star,$$

where C and $h_\star$ are constants with respect to h. The definition of a one-dimensional generalized SBP operator in the ξ_l direction, $\mathsf{D}_{\xi_l}^{(1\mathrm{D})} \in \mathbb{R}^{N_l \times N_l}$, can be found, for example, in Definition 5 in [9] and Definition 2 in [7]. To extend the various one-dimensional SBP operators (and their constituent matrices) to multiple dimensions, Kronecker tensor products are used (see, for example, Definition 1 in [7] for the definition of a Kronecker tensor product). Interpretations of the constituent matrices (e.g., H, Q_{ξ_1}) that form the various multidimensional SBP operators in terms of the different bilinear forms they approximate can be found, for example, in [6,7,5].

The focus of this paper is on element-type SBP operators, specifically, those based on LGL and LG quadratures. Table 1 in [5] lists the element-type generalized SBP operators used throughout this paper, summarizing their respective nodal distributions and accuracy properties. Finally, for the LGL and LG schemes, the numerical results are presented with respect to "Element size" by default, which is defined as follows:

$$\text{Element size} \coloneqq \left\{ \frac{N_{\text{total}}}{(p+1)^d} \right\}^{-\frac{1}{d}} = \left\{ N_{\text{elements}} \right\}^{-\frac{1}{d}},$$

where N_{total} is the total number of grid nodes and d is the number of dimensions. For the LGL and LG schemes, $N_{\text{total}} = (p+1)^d N_{\text{elements}}$, where N_{elements} is the total number of elements. When comparing the LGL and LG schemes to CSBP schemes refined by increasing the number of interior nodes for a fixed number of elements, the numerical results are presented with respect to "Grid size" to keep the comparison consistent, where Grid size $\coloneqq \{N_{\text{total}}\}^{-\frac{1}{d}}$.

3 High-order grid generation

In the present work, high-order element-type grids are constructed via element mappings. In general, on a given element, to map a point $(\xi_1, \xi_2) \in \hat{\Omega}$ in the computational domain to a point $(x_1, x_2) \in \Omega$ in the physical domain, the element-local mapping $\mathcal{T}\colon \hat{\Omega} \to \Omega$ is employed, defined by

$$\boldsymbol{x}(\boldsymbol{\xi}) = \mathcal{T}(\boldsymbol{\xi}) \coloneqq \sum_{i,j=1}^{\overline{N}} \overline{\boldsymbol{x}}_{ij} f_i(\xi_1) f_j(\xi_2), \tag{1}$$

where

$$\boldsymbol{x}(\boldsymbol{\xi}) = \begin{bmatrix} x_1(\xi_1, \xi_2) \\ x_2(\xi_1, \xi_2) \end{bmatrix} \quad \text{and} \quad \overline{\boldsymbol{x}}_{ij} = \begin{bmatrix} \overline{x}_1(i,j) \\ \overline{x}_2(i,j) \end{bmatrix}, \tag{2}$$

i.e., $\overline{\boldsymbol{x}}_{ij}$ holds the physical coordinates of the control point corresponding to the index (i, j). Furthermore, $f_i(\xi_1)$ and $f_j(\xi_2)$ represent basis functions in the ξ_1 and ξ_2 directions, respectively. Note that it has been assumed that $\overline{N}$ control points are being used in each direction. In general, the number of control points used to define the mapping will be different than the number of nodes associated with the generalized SBP operator. In this work, two approaches are used for choosing the control point locations and basis functions: one based on Lagrange polynomials and one based on B-splines. Each approach is derived starting from an existing grid consisting of structured blocks that is, in general, defined solely in terms of nonuniform nodal locations in physical space.

For the Lagrange approach, $f_i(\xi_1)$ and $f_j(\xi_2)$ are chosen to be Lagrange polynomials, i.e., $f_i(\xi_1) = \ell_i(\xi_1)$ and $f_j(\xi_2) = \ell_j(\xi_2)$, where

$$\ell_i(\xi_1) \coloneqq \prod_{\substack{m=1 \\ m \neq i}}^{\overline{N}} \frac{\xi_1 - \bar{\xi}_{1,m}}{\bar{\xi}_{1,i} - \bar{\xi}_{1,m}}, \quad i = 1, \ldots, \overline{N} \tag{3}$$

and the basis function $\ell_j(\xi_2)$ is defined similarly. The initial grid is used directly to define the control point locations $\overline{\boldsymbol{x}}_{ij}$, $i, j = 1, \ldots, \overline{N}$. Finally, for the Lagrange approach the control point $\overline{\boldsymbol{x}}_{ij}$ corresponds to the point $(\bar{\xi}_{1,i}, \bar{\xi}_{2,j})$ in computational space.

For the B-spline approach, the approach of Del Rey Fernández *et al.* [7] is followed by starting with the approach of Hicken and Zingg [16] and fitting the grid in a least-squares sense on each element to identify suitable control point locations. Formally, the control points $\overline{\boldsymbol{x}}_{ij}$, $i, j = 1, \ldots, \overline{N}$ are called de Boor control points, and $f_i(\xi_1) = \mathcal{N}_i^{(p_g+1)}(\xi_1)$ and $f_j(\xi_2) = \mathcal{N}_j^{(p_g+1)}(\xi_2)$ are B-spline basis functions.

The result of using either of the Lagrange or B-spline approaches is an element-local analytical representation of a grid that approximates the true geometry. To use a specific generalized SBP operator to numerically solve a given PDE on the resultant grid, the (ξ_1, ξ_2) nodes in computational space that correspond to the nodes of the operator of interest are determined, the (x_1, x_2) coordinates of the updated grid in physical space that corresponds to the desired generalized SBP operator are computed, and the PDE is solved numerically. With both the Lagrange and B-spline approaches, the mapping is required to be only C^0 continuous at element interfaces due to the use of SATs. However, within elements, the mapping should be at least C^p continuous, where p is the degree of generalized SBP operator being used, to avoid unnecessarily degrading the accuracy of the overall discretization. With the Lagrange approach, the mapping is C^∞ continuous within elements, which satisfies the C^p continuity requirement. With the B-spline approach, the continuity of the mapping within elements depends on the number of control points used. When $\overline{N} > p_g + 1$, the continuity of the mapping is only C^{p_g-1} at interior knots. However, when $\overline{N} = p_g + 1$, there are no interior knots (assuming open knot vectors having a multiplicity of $p_g + 1$ are used), which means that the continuity of the mapping within elements is C^∞. Therefore,

due to the C^p continuity requirement, if one wants to use a degree p_g B-spline mapping, one must use $\overline{N} = p_g + 1$ control points in each element.

Remark 1 In the context of unstructured grids, the degree of the mapping typically refers to the total degree of the mapping (e.g., [6]), while in the present multidimensional tensor-product case the degree of the mapping refers to the degree of the mapping in each coordinate direction. Therefore, a two-dimensional degree p tensor-product mapping corresponds to a mapping of total degree $2p$ in the unstructured case.

4 Accurate solutions and functionals for the linear convection equation

In this section, four dual-consistent discretizations of the two-dimensional linear convection equation are presented and characterized with respect to truncation error, solution accuracy, and functional accuracy.

4.1 Two-dimensional linear convection equation

Consider the two-dimensional linear convection equation posed as a boundary-value problem

$$\begin{aligned} \nabla \cdot \boldsymbol{\mathcal{F}} \coloneqq \sum_{m=1}^{2} \frac{\partial (a_m \mathcal{U})}{\partial x_m} = \mathcal{S} \quad & \text{in } \Omega, \\ \mathcal{U} = \mathcal{U}^- \quad & \text{on } \Gamma^-, \end{aligned} \tag{4}$$

where $\mathcal{U}$ is the solution, $\mathcal{S}$ is the source term, and a_m are the constant components of the convection speed. The inflow boundary Γ^- is defined by $\Gamma^- \coloneqq \{(x_1, x_2) \in \Gamma \mid \boldsymbol{a} \cdot \boldsymbol{n} \leq 0\}$, where $\boldsymbol{a} = [a_1, a_2]^{\mathrm{T}}$ and $\boldsymbol{n}$ is the outward unit normal vector. The outflow boundary Γ^+ is defined by $\Gamma^+ \coloneqq \Gamma \setminus \Gamma^-$.

On a single element, the transformed divergence form, or strong conservation form, of (4) is given by

$$\sum_{l=1}^{2} \frac{\partial}{\partial \xi_l} \left(\sum_{m=1}^{2} \mathcal{J} \frac{\partial \xi_l}{\partial x_m} a_m \mathcal{U} \right) = \mathcal{J} \mathcal{S} \quad \text{in } \hat{\Omega}, \tag{5}$$

where $\mathcal{J}$ is the Jacobian of the transformation from physical coordinates to computational coordinates, $\mathcal{T} \colon \hat{\Omega} \to \Omega$. See, for example, [28] for the definition of the Jacobian and the various metric terms in two dimensions. Furthermore, for simplicity, it is assumed that $\boldsymbol{a} = [1, 1]^{\mathrm{T}}$ for the presentation of the different discretizations, but $a_m \neq 1$ is introduced for the numerical examples. As noted by several papers (e.g., [7]), (5) can also be expressed in skew-symmetric form

using the canonical splitting

$$\begin{gathered}\frac{1}{2}\left\{\nabla\cdot\boldsymbol{\mathcal{F}}+\Lambda\cdot\nabla\mathcal{U}\right\}\coloneqq\\ \frac{1}{2}\sum_{l=1}^{2}\left\{\frac{\partial}{\partial\xi_l}\left(\sum_{m=1}^{2}\mathcal{J}\frac{\partial\xi_l}{\partial x_m}\mathcal{U}\right)+\sum_{m=1}^{2}\mathcal{J}\frac{\partial\xi_l}{\partial x_m}\frac{\partial\mathcal{U}}{\partial\xi_l}\right\}=\mathcal{J}\mathcal{S}\quad\text{in }\hat{\Omega},\end{gathered}\tag{6}$$

where

$$\Lambda\coloneqq\left[\sum_{m=1}^{2}\mathcal{J}\frac{\partial\xi_1}{\partial x_m},\sum_{m=1}^{2}\mathcal{J}\frac{\partial\xi_2}{\partial x_m}\right]^{\mathrm{T}}.$$

While the skew-symmetric form has been shown to be important for constructing provably stable schemes (see, for example, [7]), in the present work discretizations of both forms are examined with respect to dual consistency and functional superconvergence, in part because discretizations approximating the divergence form of the governing equations are still used in many production CFD codes.

4.2 Corresponding continuous dual equation

To derive the continuous dual equation for both the divergence and the skew-symmetric forms of the linear convection equation, the following integral functional is introduced that takes the given form when one assumes that the domain consists of a single element:

$$\mathcal{I}(\mathcal{U})\coloneqq\int_{\hat{\Omega}}\mathcal{J}\mathcal{G}\mathcal{U}\,d\hat{\Omega}+\int_{\hat{\Gamma}^{+}}\psi_{\hat{\Gamma}}\,\boldsymbol{n}\cdot(\Lambda\mathcal{U})\,d\hat{\Gamma},\tag{7}$$

which has a contribution from the volume of the domain and a contribution from the outflow boundary of the domain, denoted by $\hat{\Gamma}^{+}$. Following a procedure similar to that in [13], the dual problem can be expressed in both divergence and skew-symmetric forms analogous to the primal problem:

$$-\Lambda\cdot\nabla\psi=\mathcal{J}\mathcal{G}\quad\text{and}\quad-\frac{1}{2}\left\{\Lambda\cdot\nabla\psi+\nabla\cdot(\Lambda\psi)\right\}=\mathcal{J}\mathcal{G}.$$

Like the primal problem, the divergence and skew-symmetric forms of the dual problem are analytically identical—only when discretized are the two forms no longer identical.

4.3 Discretizations of the two-dimensional linear convection equation

In the following sections, two discretizations of the divergence form of the linear convection equation and two discretizations of the skew-symmetric form of the linear convection equation are presented. Each discretization is based on either the mortar-element approach or the global SBP-operator approach as

described in Del Rey Fernández *et al.* [7]. For the mortar-element approach, the surface quadrature nodes are defined on mortar faces that are introduced at element interfaces and boundaries and the grid metrics are defined on the mortar faces. In contrast, for the global SBP-operator approach, a global SBP operator is constructed over the entire grid, no mortar faces are introduced, and the grid metrics are approximated using the global SBP operators. For each scheme, a discrete integral functional is defined that approximates the continuous integral functional and a discretization is derived that approximates the corresponding dual problem. For simplicity, each discretization is constructed for a domain consisting of only a single element, which eliminates the need for an element index. Interface SATs for these types of schemes are discussed in [7].

4.3.1 Mortar-element approach: divergence form

First, the divergence form of the linear convection equation, given by (5), is discretized using the mortar-element approach. This gives, on a single element,

$$\sum_{l,m=1}^{2} \mathsf{D}_{\xi_l} \operatorname{diag}\left(\mathcal{J}\frac{\partial \xi_l}{\partial x_m}\right)_h \boldsymbol{u}_h = \operatorname{diag}\left(\mathcal{J}_h\right)\boldsymbol{s} + \mathrm{SAT}^{\boldsymbol{u}_h}_{(2l-1)} + \mathrm{SAT}^{\boldsymbol{u}_h}_{(2l)}, \tag{8}$$

where the boundary SAT on the $2l-1$ face is defined as

$$\mathrm{SAT}^{\boldsymbol{u}_h}_{(2l-1)} \coloneqq \mathsf{H}^{-1}\sum_{l=1}^{2}\left\{-\mathsf{R}^{\mathrm{T}}_{\alpha_{\xi_l}}\mathsf{H}^{\perp}_{\xi_l}\left(\boldsymbol{f}_{(2l-1),h}(\boldsymbol{u}_h) - \boldsymbol{f}^{\star}_{(2l-1),h}(\boldsymbol{u}_h)\right)\right\}$$

with

$$\boldsymbol{f}_{(2l-1),h}(\boldsymbol{u}_h) \coloneqq \sum_{m=1}^{2}\mathsf{R}_{\alpha_{\xi_l}}\operatorname{diag}\left(\mathcal{J}\frac{\partial \xi_l}{\partial x_m}\right)_h \boldsymbol{u}_h$$

and

$$\begin{aligned}\boldsymbol{f}^{\star}_{(2l-1),h}(\boldsymbol{u}_h) \coloneqq{}& \frac{1}{2}\mathsf{\Lambda}_{(2l-1),h}\left(\boldsymbol{u}_{[2l-1]} + \mathsf{R}_{\alpha_{\xi_l}}\boldsymbol{u}_h\right)\\ &- \frac{1}{2}\left|\mathsf{\Lambda}_{(2l-1),h}\right|\left(\mathsf{R}_{\alpha_{\xi_l}}\boldsymbol{u}_h - \boldsymbol{u}_{[2l-1]}\right).\end{aligned}$$

The boundary SAT and fluxes on the $2l$ face are defined similarly. The volume metric terms and metric Jacobians are stored in the diagonal matrices

$$\operatorname{diag}\left(\mathcal{J}\frac{\partial \xi_l}{\partial x_m}\right)_h \quad \text{and} \quad \operatorname{diag}\left(\mathcal{J}_h\right),$$

respectively, where the subscript h indicates that these terms are, in general, approximate terms. Similarly, the metric terms appearing in the SAT on the $2l-1$ face, for example, are the mortar metric terms given by

$$\mathsf{\Lambda}_{(2l-1),h} \coloneqq \sum_{m=1}^{2}\operatorname{diag}\left(\mathcal{J}\frac{\partial \xi_l}{\partial x_m}\right)^{[2l-1]}_h,$$

where the quantity within the square brackets on a given mortar metric term indicates the surface on which that specific metric term is constructed. Similarly, the vectors $\boldsymbol{u}_{[2l-1]}$ and $\boldsymbol{u}_{[2l]}$ hold, in the single element case, boundary data on the $2l-1$ face and the $2l$ face, respectively. The discrete integral functional is given by

$$\begin{aligned}\mathcal{I}_h(\boldsymbol{u}_h) \coloneqq \boldsymbol{g}^{\mathrm{T}}\mathsf{H}\,\mathrm{diag}\left(\mathcal{J}_h\right)\boldsymbol{u}_h \\ - \frac{1}{2}\sum_{l=1}^{2}\boldsymbol{\psi}_{[2l-1]}^{\mathrm{T}}\mathsf{H}_{\xi_l}^{\perp}\left(\Lambda_{(2l-1),h} - \left|\Lambda_{(2l-1),h}\right|\right)\mathsf{R}_{\alpha_{\xi_l}}\boldsymbol{u}_h \\ + \frac{1}{2}\sum_{l=1}^{2}\boldsymbol{\psi}_{[2l]}^{\mathrm{T}}\mathsf{H}_{\xi_l}^{\perp}\left(\Lambda_{(2l),h} + \left|\Lambda_{(2l),h}\right|\right)\mathsf{R}_{\beta_{\xi_l}}\boldsymbol{u}_h.\end{aligned} \tag{9}$$

The discrete dual problem is constructed by linearizing the discrete residual and the discrete integral functional as follows (see, for example, Hartmann [13]): find $\boldsymbol{\psi}_h \in \mathbb{R}^n$ such that

$$\mathcal{R}_h'[\boldsymbol{u}_h](\boldsymbol{w}_h, \boldsymbol{\psi}_h) = \mathcal{I}_h'[\boldsymbol{u}_h](\boldsymbol{w}_h) \quad \forall \boldsymbol{w}_h \in \mathbb{R}^n, \tag{10}$$

where $\mathcal{R}_h'[\boldsymbol{u}_h](\boldsymbol{w}_h, \boldsymbol{\psi}_h)$ is the Fréchet derivative of $\mathcal{R}_h(\cdot, \boldsymbol{\psi}_h)$ at $\boldsymbol{u}_h$ in the direction $\boldsymbol{w}_h$, $\mathcal{I}_h'[\boldsymbol{u}_h](\boldsymbol{w}_h)$ is the Fréchet derivative of $\mathcal{I}_h(\cdot)$ at $\boldsymbol{u}_h$ in the direction $\boldsymbol{w}_h$, and n is the number of nodes. As the linear convection equation is a linear PDE, the use of Fréchet derivatives in the definition of the discrete dual problem might not be strictly necessary in all cases; however, in the present case it facilitates the extension of the approach to nonlinear PDEs.

For the present discretization, the evaluation of (10) leads to the following discrete dual problem

$$-\sum_{l,m=1}^{2}\mathrm{diag}\left(\mathcal{J}\frac{\partial \xi_l}{\partial x_m}\right)_h \mathsf{D}_{\xi_l}\boldsymbol{\psi}_h = \mathrm{diag}\left(\mathcal{J}_h\right)\boldsymbol{g} + \mathrm{SAT}_{(2l-1)}^{\boldsymbol{\psi}_h} + \mathrm{SAT}_{(2l)}^{\boldsymbol{\psi}_h}, \tag{11}$$

where the boundary SAT on the $2l-1$ face, for example, is given by

$$\begin{aligned}\mathrm{SAT}_{(2l-1)}^{\boldsymbol{\psi}_h} \coloneqq \mathsf{H}^{-1}\sum_{l=1}^{2}\left\{\boldsymbol{f}_{(2l-1),h}^{\star\prime}[\boldsymbol{u}_h]\right\}^{\mathrm{T}}\mathsf{H}_{\xi_l}^{\perp}\mathsf{R}_{\alpha_{\xi_l}}\boldsymbol{\psi}_h \\ - \frac{1}{2}\mathsf{H}^{-1}\sum_{l=1}^{2}\mathsf{R}_{\alpha_{\xi_l}}^{\mathrm{T}}\mathsf{H}_{\xi_l}^{\perp}\left(\Lambda_{(2l-1),h} - \left|\Lambda_{(2l-1),h}\right|\right)\boldsymbol{\psi}_{[2l-1]}.\end{aligned}$$

Like $\boldsymbol{u}_{[2l-1]}$ and $\boldsymbol{u}_{[2l]}$, the vectors $\boldsymbol{\psi}_{[2l-1]}$ and $\boldsymbol{\psi}_{[2l]}$ hold, in the single element case, boundary data on the $2l-1$ face and the $2l$ face, respectively.

4.3.2 Mortar-element approach: skew-symmetric form

Next, the skew-symmetric form of the linear convection equation given by (6) is discretized using the mortar-element approach. This gives, on a single element,

$$\begin{aligned}\frac{1}{2}\sum_{l,m=1}^{2}\left\{\mathsf{D}_{\xi_l}\operatorname{diag}\left(\mathcal{J}\frac{\partial\xi_l}{\partial x_m}\right)_h\boldsymbol{u}_h+\operatorname{diag}\left(\mathcal{J}\frac{\partial\xi_l}{\partial x_m}\right)_h\mathsf{D}_{\xi_l}\boldsymbol{u}_h\right\}=\\ \operatorname{diag}\left(\mathcal{J}_h\right)\boldsymbol{s}+\mathrm{SAT}^{\boldsymbol{u}_h}_{(2l-1)}+\mathrm{SAT}^{\boldsymbol{u}_h}_{(2l)},\end{aligned}\tag{12}$$

where the general structures of the boundary SATs are unchanged from the mortar-element discretization of the divergence form in addition to the discrete integral functional. Likewise, the fluxes in the boundary SATs are the same as for the mortar-element discretization of the divergence form; however, the numerical fluxes are not. For (12), the numerical flux in the boundary SAT on the $2l-1$ face, for example, is defined by

$$\begin{aligned}\boldsymbol{f}^{\star}_{(2l-1),h}(\boldsymbol{u}_h)\coloneqq\frac{1}{2}\left(\Lambda_{(2l-1),h}\boldsymbol{u}_{[2l-1]}+\mathsf{R}_{\alpha_{\xi_l}}\sum_{m=1}^{2}\operatorname{diag}\left(\mathcal{J}\frac{\partial\xi_l}{\partial x_m}\right)_h\boldsymbol{u}_h\right)\\ -\frac{1}{2}\left|\Lambda_{(2l-1),h}\right|\left(\mathsf{R}_{\alpha_{\xi_l}}\boldsymbol{u}_h-\boldsymbol{u}_{[2l-1]}\right).\end{aligned}$$

The corresponding discrete dual problem is given by

$$\begin{aligned}-\frac{1}{2}\sum_{l,m=1}^{2}\left\{\mathsf{D}_{\xi_l}\operatorname{diag}\left(\mathcal{J}\frac{\partial\xi_l}{\partial x_m}\right)_h+\operatorname{diag}\left(\mathcal{J}\frac{\partial\xi_l}{\partial x_m}\right)_h\mathsf{D}_{\xi_l}\right\}\boldsymbol{\psi}_h=\\ \operatorname{diag}\left(\mathcal{J}_h\right)\boldsymbol{g}+\mathrm{SAT}^{\boldsymbol{\psi}_h}_{(2l-1)}+\mathrm{SAT}^{\boldsymbol{\psi}_h}_{(2l)},\end{aligned}\tag{13}$$

where the boundary SAT on the $2l-1$ face, for example, is given by

$$\begin{aligned}\mathrm{SAT}^{\boldsymbol{\psi}_h}_{(2l-1)}\coloneqq&\frac{1}{2}\mathsf{H}^{-1}\sum_{l=1}^{2}\mathsf{R}^{\mathrm{T}}_{\alpha_{\xi_l}}\mathsf{H}^{\perp}_{\xi_l}\mathsf{R}_{\alpha_{\xi_l}}\sum_{m=1}^{2}\operatorname{diag}\left(\mathcal{J}\frac{\partial\xi_l}{\partial x_m}\right)_h\boldsymbol{\psi}_h\\ &-\frac{1}{2}\mathsf{H}^{-1}\sum_{l=1}^{2}\sum_{m=1}^{2}\operatorname{diag}\left(\mathcal{J}\frac{\partial\xi_l}{\partial x_m}\right)_h\mathsf{R}^{\mathrm{T}}_{\alpha_{\xi_l}}\mathsf{H}^{\perp}_{\xi_l}\mathsf{R}_{\alpha_{\xi_l}}\boldsymbol{\psi}_h\\ &+\mathsf{H}^{-1}\sum_{l=1}^{2}\left\{\boldsymbol{f}^{\star\prime}_{(2l-1),h}[\boldsymbol{u}_h]\right\}^{\mathrm{T}}\mathsf{H}^{\perp}_{\xi_l}\mathsf{R}_{\alpha_{\xi_l}}\boldsymbol{\psi}_h\\ &-\frac{1}{2}\mathsf{H}^{-1}\sum_{l=1}^{2}\mathsf{R}^{\mathrm{T}}_{\alpha_{\xi_l}}\mathsf{H}^{\perp}_{\xi_l}\left(\Lambda_{(2l-1),h}-\left|\Lambda_{(2l-1),h}\right|\right)\boldsymbol{\psi}_{[2l-1]}.\end{aligned}$$

4.3.3 Global SBP-operator approach: divergence form

Next, the divergence form of the linear convection equation, given by (5), is discretized using the global SBP-operator approach. This gives, on a single element,

$$\sum_{l,m=1}^{2} \mathsf{D}_{\xi_l} \operatorname{diag}\left(\mathcal{J}\frac{\partial \xi_l}{\partial x_m}\right)_h \boldsymbol{u}_h = \operatorname{diag}\left(\mathcal{J}_h\right)\boldsymbol{s} + \mathrm{SAT}^{\boldsymbol{u}_h}_{(2l-1)} + \mathrm{SAT}^{\boldsymbol{u}_h}_{(2l)} \tag{14}$$

where the boundary SAT on the $2l-1$ face, for example, is defined by

$$\mathrm{SAT}^{\boldsymbol{u}_h}_{(2l-1)} \coloneqq -\frac{1}{2}\mathsf{H}^{-1}\sum_{l=1}^{2}\left\{\mathsf{R}^{\mathrm{T}}_{\alpha_{\xi_l}}\mathsf{H}^{\perp}_{\xi_l}\mathsf{R}_{\alpha_{\xi_l}}\left(\Lambda_{h,l}+|\Lambda_{h,l}|\right)\right\}\left(\boldsymbol{u}_h - \tilde{\mathsf{I}}_{\xi_l}\boldsymbol{u}_{[2l-1]}\right),$$

where

$$\Lambda_{h,l} \coloneqq \sum_{m=1}^{2}\operatorname{diag}\left(\mathcal{J}\frac{\partial \xi_l}{\partial x_m}\right)_h,$$

$\tilde{\mathsf{I}}_{\xi_1} \coloneqq \mathbf{1}_{\xi_1}\otimes \mathsf{I}_{\xi_2}$, and $\tilde{\mathsf{I}}_{\xi_2} \coloneqq \mathsf{I}_{\xi_1}\otimes \mathbf{1}_{\xi_2}$ have been introduced. The discrete integral functional is given by

$$\begin{aligned}\mathcal{I}_h(\boldsymbol{u}_h) \coloneqq\ & \boldsymbol{g}^{\mathrm{T}}\mathsf{H}\operatorname{diag}\left(\mathcal{J}_h\right)\boldsymbol{u}_h \\ & - \frac{1}{2}\sum_{l=1}^{2}\boldsymbol{\psi}^{\mathrm{T}}_{[2l-1]}\mathsf{H}^{\perp}_{\xi_l}\mathsf{R}_{\alpha_{\xi_l}}\left(\Lambda_{h,l}-|\Lambda_{h,l}|\right)\boldsymbol{u}_h \\ & + \frac{1}{2}\sum_{l=1}^{2}\boldsymbol{\psi}^{\mathrm{T}}_{[2l]}\mathsf{H}^{\perp}_{\xi_l}\mathsf{R}_{\beta_{\xi_l}}\left(\Lambda_{h,l}+|\Lambda_{h,l}|\right)\boldsymbol{u}_h.\end{aligned} \tag{15}$$

This leads to the following discrete dual problem

$$-\sum_{l,m=1}^{2}\operatorname{diag}\left(\mathcal{J}\frac{\partial \xi_l}{\partial x_m}\right)_h \mathsf{D}_{\xi_l}\boldsymbol{\psi}_h = \operatorname{diag}\left(\mathcal{J}_h\right)\boldsymbol{g} + \mathrm{SAT}^{\boldsymbol{\psi}_h}_{(2l-1)} + \mathrm{SAT}^{\boldsymbol{\psi}_h}_{(2l)}, \tag{16}$$

where the boundary SAT on the $2l-1$ face, for example, is given by

$$\mathrm{SAT}^{\boldsymbol{\psi}_h}_{(2l-1)} \coloneqq \frac{1}{2}\mathsf{H}^{-1}\sum_{l=1}^{2}\left\{\left(\Lambda_{h,l}-|\Lambda_{h,l}|\right)\mathsf{R}^{\mathrm{T}}_{\alpha_{\xi_l}}\mathsf{H}^{\perp}_{\xi_l}\mathsf{R}_{\alpha_{\xi_l}}\right\}\left(\boldsymbol{\psi}_h - \tilde{\mathsf{I}}_{\xi_l}\boldsymbol{\psi}_{[2l-1]}\right).$$

4.3.4 Global SBP-operator approach: skew-symmetric form

Here, the skew-symmetric form of the linear convection equation given by (6) is discretized using the global SBP-operator approach. This gives, on a single element,

$$\begin{aligned}\frac{1}{2}\sum_{l,m=1}^{2}\left\{\mathsf{D}_{\xi_l}\operatorname{diag}\left(\mathcal{J}\frac{\partial \xi_l}{\partial x_m}\right)_h \boldsymbol{u}_h + \operatorname{diag}\left(\mathcal{J}\frac{\partial \xi_l}{\partial x_m}\right)_h \mathsf{D}_{\xi_l}\boldsymbol{u}_h\right\} = \\ \operatorname{diag}\left(\mathcal{J}_h\right)\boldsymbol{s} + \mathrm{SAT}^{\boldsymbol{u}_h}_{(2l-1)} + \mathrm{SAT}^{\boldsymbol{u}_h}_{(2l)},\end{aligned} \tag{17}$$

where the boundary SAT on the $2l-1$ face, for example, is defined by

$$\begin{aligned}
&\mathrm{SAT}^{\boldsymbol{u}_h}_{(2l-1)} \coloneqq \\
&-\frac{1}{2}\mathsf{H}^{-1}\sum_{l=1}^{2}\left\{\frac{1}{2}\mathsf{R}^{\mathrm{T}}_{\alpha_{\xi_l}}\mathsf{H}^{\perp}_{\xi_l}\mathsf{R}_{\alpha_{\xi_l}}\left(\Lambda_{h,l}+|\Lambda_{h,l}|\right)+\frac{1}{2}\left(\Lambda_{h,l}+|\Lambda_{h,l}|\right)\mathsf{R}^{\mathrm{T}}_{\alpha_{\xi_l}}\mathsf{H}^{\perp}_{\xi_l}\mathsf{R}_{\alpha_{\xi_l}}\right\} \\
&\times\left(\boldsymbol{u}_h-\tilde{\mathsf{I}}_{\xi_l}\boldsymbol{u}_{[2l-1]}\right).
\end{aligned}$$

The discrete integral functional is given by

$$\begin{aligned}
\mathcal{I}_h(\boldsymbol{u}_h) \coloneqq\ & \boldsymbol{g}^{\mathrm{T}}\mathsf{H}\,\mathrm{diag}\left(\mathcal{J}_h\right)\boldsymbol{u}_h \\
&-\frac{1}{2}\sum_{l=1}^{2}\left\{\frac{1}{2}\left(\tilde{\mathsf{I}}_{\xi_l}\boldsymbol{\psi}_{[2l-1]}\right)^{\mathrm{T}}\mathsf{R}^{\mathrm{T}}_{\alpha_{\xi_l}}\mathsf{H}^{\perp}_{\xi_l}\mathsf{R}_{\alpha_{\xi_l}}\left(\Lambda_{h,l}-|\Lambda_{h,l}|\right)\boldsymbol{u}_h\right. \\
&\left.+\frac{1}{2}\left(\left(\Lambda_{h,l}-|\Lambda_{h,l}|\right)\tilde{\mathsf{I}}_{\xi_l}\boldsymbol{\psi}_{[2l-1]}\right)^{\mathrm{T}}\mathsf{R}^{\mathrm{T}}_{\alpha_{\xi_l}}\mathsf{H}^{\perp}_{\xi_l}\mathsf{R}_{\alpha_{\xi_l}}\boldsymbol{u}_h\right\} \\
&+\frac{1}{2}\sum_{l=1}^{2}\left\{\frac{1}{2}\left(\tilde{\mathsf{I}}_{\xi_l}\boldsymbol{\psi}_{[2l]}\right)^{\mathrm{T}}\mathsf{R}^{\mathrm{T}}_{\beta_{\xi_l}}\mathsf{H}^{\perp}_{\xi_l}\mathsf{R}_{\beta_{\xi_l}}\left(\Lambda_{h,l}+|\Lambda_{h,l}|\right)\boldsymbol{u}_h\right. \\
&\left.+\frac{1}{2}\left(\left(\Lambda_{h,l}+|\Lambda_{h,l}|\right)\tilde{\mathsf{I}}_{\xi_l}\boldsymbol{\psi}_{[2l]}\right)^{\mathrm{T}}\mathsf{R}^{\mathrm{T}}_{\beta_{\xi_l}}\mathsf{H}^{\perp}_{\xi_l}\mathsf{R}_{\beta_{\xi_l}}\boldsymbol{u}_h\right\}.
\end{aligned} \tag{18}$$

This leads to the following discrete dual problem

$$\begin{aligned}
-\frac{1}{2}\sum_{l,m=1}^{2}\left\{\mathsf{D}_{\xi_l}\,\mathrm{diag}\left(\mathcal{J}\frac{\partial\xi_l}{\partial x_m}\right)_h+\mathrm{diag}\left(\mathcal{J}\frac{\partial\xi_l}{\partial x_m}\right)_h\mathsf{D}_{\xi_l}\right\}\boldsymbol{\psi}_h = \\
\mathrm{diag}\left(\mathcal{J}_h\right)\boldsymbol{g}+\mathrm{SAT}^{\boldsymbol{\psi}_h}_{(2l-1)}+\mathrm{SAT}^{\boldsymbol{\psi}_h}_{(2l)}
\end{aligned} \tag{19}$$

where the boundary SAT on the $2l-1$ face, for example, is defined by

$$\begin{aligned}
&\mathrm{SAT}^{\boldsymbol{\psi}_h}_{(2l-1)} \coloneqq \\
&\frac{1}{2}\mathsf{H}^{-1}\sum_{l=1}^{2}\left\{\frac{1}{2}\mathsf{R}^{\mathrm{T}}_{\alpha_{\xi_l}}\mathsf{H}^{\perp}_{\xi_l}\mathsf{R}_{\alpha_{\xi_l}}\left(\Lambda_{h,l}-|\Lambda_{h,l}|\right)+\frac{1}{2}\left(\Lambda_{h,l}-|\Lambda_{h,l}|\right)\mathsf{R}^{\mathrm{T}}_{\alpha_{\xi_l}}\mathsf{H}^{\perp}_{\xi_l}\mathsf{R}_{\alpha_{\xi_l}}\right\} \\
&\times\left(\boldsymbol{\psi}_h-\tilde{\mathsf{I}}_{\xi_l}\boldsymbol{\psi}_{[2l-1]}\right).
\end{aligned}$$

4.4 Approximations of the metrics

To derive the transformed version of the linear convection equation in computational coordinates, the volume metric invariants are used, given by

$$\sum_{l=1}^{2}\frac{\partial}{\partial\xi_l}\left(\mathcal{J}\frac{\partial\xi_l}{\partial x_m}\right)=0,\quad m=1,2. \tag{20}$$

Also, note that by integrating the volume metric invariants over the domain the surface metric invariants are obtained, given by

$$\int_{\hat{\Omega}} \sum_{l=1}^{2} \frac{\partial}{\partial \xi_l} \left(\mathcal{J} \frac{\partial \xi_l}{\partial x_m} \right) d\hat{\Omega} = \oint_{\hat{\Gamma}} \sum_{l=1}^{2} \left(\mathcal{J} \frac{\partial \xi_l}{\partial x_m} \right) n_{\xi_l} \, d\hat{\Gamma} = 0, \quad m = 1, 2. \tag{21}$$

Discretely satisfying the metric invariants is important for freestream preservation [7]. Therefore, approximations of the metric terms are sought that satisfy discrete versions of the metric invariants.

4.4.1 Mortar-element metrics

Substituting the constant solution $\boldsymbol{u}_{h,\kappa} = \mathbf{1}_\kappa$ into the mortar-element discretizations of the skew-symmetric and divergence forms of the linear convection equation, the following discretization of the volume metric invariants on element κ is obtained:

$$\begin{aligned} &\sum_{l=1}^{2} \mathsf{D}_{\xi_l} \operatorname{diag} \left(\mathcal{J} \frac{\partial \xi_l}{\partial x_m} \right)_{h,\kappa} \mathbf{1}_\kappa = \\ &\mathsf{H}^{-1} \sum_{l=1}^{2} \left\{ \mathsf{E}_{\xi_l} \operatorname{diag} \left(\mathcal{J} \frac{\partial \xi_l}{\partial x_m} \right)_{h,\kappa} \mathbf{1}_\kappa + \mathsf{R}_{\alpha_{\xi_l}}^{\mathrm{T}} \mathsf{H}_{\xi_l}^{\perp} \operatorname{diag} \left(\mathcal{J} \frac{\partial \xi_l}{\partial x_m} \right)_{h,\kappa}^{[2l-1]} \mathbf{1}_{[2l-1]} \right. \\ &\left. - \mathsf{R}_{\beta_{\xi_l}}^{\mathrm{T}} \mathsf{H}_{\xi_l}^{\perp} \operatorname{diag} \left(\mathcal{J} \frac{\partial \xi_l}{\partial x_m} \right)_{h,\kappa}^{[2l]} \mathbf{1}_{[2l]} \right\}, \quad m = 1, 2. \end{aligned} \tag{22}$$

Furthermore, discretely integrating the discrete volume metric invariants over the domain by premultiplying by $\mathbf{1}_\kappa^{\mathrm{T}} \mathsf{H}$ and using the SBP property results in a discrete approximation of the surface metric invariants.

As the baseline approach, the volume metric terms are approximated using the same SBP operator used to discretize the flux terms and the surface metric terms are constructed by extrapolating the volume metric terms to the surface of each element. For operators with boundary nodes in two-dimensions, the standard approach for the metrics leads to the satisfaction of the discrete volume and surface metric invariants. However, as noted in [7], for operators without boundary nodes, the metric values extrapolated from adjacent elements to a shared surface will not coincide in general (this occurs in two dimensions when $p_g \geq p + 1$).

Alternatively, a modified approach for the mortar-element metrics can be used, which is the same as that used by Crean *et al.* [6] in a multidimensional setting and Del Rey Fernández *et al.* [7] in a tensor-product setting. With this approach, the volume metrics on element κ are determined by solving a strictly convex quadratic optimization problem, namely

$$\begin{aligned} &\min_{\boldsymbol{a}_m^\kappa} \frac{1}{2} \left(\boldsymbol{a}_m^\kappa - \boldsymbol{a}_{m,\text{target}}^\kappa \right)^{\mathrm{T}} \left(\boldsymbol{a}_m^\kappa - \boldsymbol{a}_{m,\text{target}}^\kappa \right), \\ &\text{subject to } \mathsf{M} \boldsymbol{a}_m^\kappa = \boldsymbol{c}_m^\kappa, \; m = 1, 2, \end{aligned} \tag{23}$$

where

$$(\boldsymbol{a}_m^\kappa)^{\mathrm{T}} \coloneqq \mathbf{1}_\kappa^{\mathrm{T}} \left[\mathrm{diag}\left(\mathcal{J} \tfrac{\partial \xi_1}{\partial x_m} \right)_{h,\kappa}, \mathrm{diag}\left(\mathcal{J} \tfrac{\partial \xi_2}{\partial x_m} \right)_{h,\kappa}, \mathrm{diag}\left(\mathcal{J} \tfrac{\partial \xi_3}{\partial x_m} \right)_{h,\kappa} \right]. \quad (24)$$

The entries in $\boldsymbol{a}_{m,\mathrm{target}}^\kappa$ are taken from the analytical mapping, while the constraint $\mathsf{M}\boldsymbol{a}_m^\kappa = \boldsymbol{c}_m^\kappa$ arises from the discretization of the volume metric invariants on element κ. The solution to the optimization problem is given by (see Proposition 1 in Crean *et al.* [6])

$$\boldsymbol{a}_m^\kappa = \boldsymbol{a}_{m,\mathrm{target}}^\kappa + \mathsf{M}^\dagger \left(\mathsf{M}\boldsymbol{a}_{m,\mathrm{target}}^\kappa - \boldsymbol{c}_m^\kappa \right), \quad (25)$$

where $\mathsf{M}^\dagger$ is the Moore-Penrose pseudoinverse of M. As articulated in [7], to solve the optimization problem for the metrics given by (23), the condition $\mathbf{1}_\kappa^{\mathrm{T}} \boldsymbol{c}_m^\kappa = 0$ is required, which is the discrete analogue of the continuous surface metric invariant condition on element κ. The condition $\mathbf{1}_\kappa^{\mathrm{T}} \boldsymbol{c}_m^\kappa = 0$ is satisfied if the surface metric terms appearing in $\boldsymbol{c}_m^\kappa$ are taken directly from a polynomial curvilinear coordinate transformation and the degree of the transformation leads to surface metric terms whose degree is less than or equal to the degree of the quadrature associated with the SBP operator being used.

Remark 2 In general, one does not need to restrict oneself to a certain degree of polynomial curvilinear coordinate transformation to use the modified approach for the metrics. Indeed, there is no need to assume that the curvilinear coordinate transformation has any polynomial properties at all. As alluded to by Crean *et al.* [6], in the general case, one can first solve a global optimization problem for the surface metrics appearing in $\boldsymbol{c}_m^\kappa$ for each element such that the condition $\mathbf{1}_\kappa^{\mathrm{T}} \boldsymbol{c}_m^\kappa = 0$ is satisfied on each element. Following this global optimization, the modified approach for the metrics can be used to solve for the volume metrics on each element.

4.4.2 Global SBP-operator metrics

For the global SBP-operator approaches, the metrics are approximated using the global operators with one of the standard approaches. In two dimensions, this process is straightforward. In three dimensions, there are more possibilities. In Del Rey Fernández *et al.* [7], an example using the approach of Thomas and Lombard [30] is given. Other standard approaches include those given by Deng *et al.* [11] and Vinokur and Yee [32].

4.5 Numerical results

In this section the results of numerical experiments exploring the properties of the various schemes are presented, with a particular focus on dual consistency and functional superconvergence.

4.5.1 Two-dimensional scalar linear boundary-value problem

The steady two-dimensional linear convection equation is considered over a unit square, and the primal and dual source terms, denoted by $\mathcal{S} = \mathcal{S}(x, y)$ and $\mathcal{G} = \mathcal{G}(x, y)$, respectively, are chosen such that the exact primal and dual solutions are defined by

$$\begin{aligned} \mathcal{U}_{\text{exact}}(x, y) &\coloneqq \sin(2\pi x) + \sin(2\pi y) \text{ and} \\ \psi_{\text{exact}}(x, y) &\coloneqq \sin(2\pi x) + \frac{\exp(y) - 1}{\exp(1) - 1}, \end{aligned}$$

respectively. These particular primal and dual solutions ensure that both the volume and boundary contributions to the integral functional (7) are nonzero. The initial grid is constructed via the following analytical transformation,

$$\begin{aligned} x(\xi, \eta) &= \xi + \frac{1}{40} \sin(2\pi\xi) \sin(2\pi\eta), \\ y(\xi, \eta) &= \eta + \frac{1}{40} \frac{\exp(\xi) - 1}{\exp(1) - 1} \sin(2\pi\eta), \end{aligned}$$

where $(\xi, \eta) \in \Omega$. The Lagrange approach for constructing high-order grids outlined in Section 3 is used together with the exact analytical transformation above to generate the grids for the numerical experiments summarized in this section. Each of the four primal and dual discretizations from Section 4 can be written in the following compact forms,

$$\begin{aligned} \mathsf{A}_g \boldsymbol{u}_{h,g} &= \boldsymbol{f}_g, \\ \mathsf{A}_g^{\mathrm{T}} \boldsymbol{\psi}_{h,g} &= \boldsymbol{f}_g^{\text{dual}}, \end{aligned}$$

where $\boldsymbol{u}_{h,g}$ and $\boldsymbol{\psi}_{h,g}$ are the global primal and dual solution vectors, respectively, A_g and $\mathsf{A}_g^{\mathrm{T}}$ are the primal and dual system matrices, respectively, and $\boldsymbol{f}_g$ and $\boldsymbol{f}_g^{\text{dual}}$ are the primal and dual load vectors, respectively. The discrete primal functional $\mathcal{I}_h(\boldsymbol{u}_{h,g})$ for each scheme is computed from either (9), (15), or (18), depending on the discretization, and the discrete dual functional for each scheme is computed from

$$\mathcal{I}_h(\boldsymbol{\psi}_{h,g}) \coloneqq \boldsymbol{\psi}_{h,g}^{\mathrm{T}} \boldsymbol{f}_g,$$

where $\mathcal{I}_h(\boldsymbol{u}_{h,g}) = \mathcal{I}_h(\boldsymbol{\psi}_{h,g})$ by construction. To evaluate the accuracy of each scheme, the six accuracy measures summarized in Table 1 are used. The truncation error should be $\mathcal{O}(h^p)$ to confirm that the primal and dual discretizations are consistent and dual consistent, respectively. The solution error should be at least $\mathcal{O}(h^p)$ with $\mathcal{O}(h^{p+1})$ often being observed in the literature. Finally, the functional error is considered to be superconvergent if it is at least $\mathcal{O}(h^{2p})$ and anything less is considered suboptimal.

Table 2 summarizes the test case parameters considered for the boundary value problem governed by the linear convection equation. For each case listed

Table 1: Accuracy measures for the linear convection equation.

Accuracy measure	**Definition**
Primal truncation error	$\left\|\mathsf{J}_g^{-1}\mathsf{H}_g^{-1}(\mathsf{A}_g\boldsymbol{u}_g - \mathcal{F}_g)\right\|_\infty = \max\left\|\mathsf{J}_g^{-1}\mathsf{H}_g^{-1}(\mathsf{A}_g\boldsymbol{u}_g - \mathcal{F}_g)\right\|$
Primal solution error	$\left\|\boldsymbol{u}_{h,g} - \boldsymbol{u}_g\right\|_{\mathsf{H}_g} = \sqrt{(\boldsymbol{u}_{h,g} - \boldsymbol{u}_g)^{\mathrm{T}}\mathsf{H}_g(\boldsymbol{u}_{h,g} - \boldsymbol{u}_g)}$
Primal functional error	$\left\|\mathcal{I}_h(\boldsymbol{u}_{h,g}) - \mathcal{I}(\mathcal{U})\right\|$
Dual truncation error	$\left\|\mathsf{J}_g^{-1}\mathsf{H}_g^{-1}(\mathsf{A}_g^{\mathrm{T}}\boldsymbol{\psi}_g - \mathcal{F}_g^{\mathrm{dual}})\right\|_\infty = \max\left\|\mathsf{J}_g^{-1}\mathsf{H}_g^{-1}(\mathsf{A}_g^{\mathrm{T}}\boldsymbol{\psi}_g - \mathcal{F}_g^{\mathrm{dual}})\right\|$
Dual solution error	$\left\|\boldsymbol{\psi}_{h,g} - \boldsymbol{\psi}_g\right\|_{\mathsf{H}_g} = \sqrt{(\boldsymbol{\psi}_{h,g} - \boldsymbol{\psi}_g)^{\mathrm{T}}\mathsf{H}_g(\boldsymbol{\psi}_{h,g} - \boldsymbol{\psi}_g)}$
Dual functional error	$\left\|\mathcal{I}_h(\boldsymbol{\psi}_{h,g}) - \mathcal{I}(\psi)\right\|$

Table 2: Test case matrix for the boundary-value problem governed by the linear convection equation.

Type of discretization	**Form of equation**	**Metrics**	**Mapping**	p_g
Mortar-element	Divergence	Baseline	Lagrange	p
Mortar-element	Divergence	Baseline	Lagrange	$p+1$
Mortar-element	Divergence	Modified	Lagrange	$p+1$
Mortar-element	Skew-symmetric	Baseline	Lagrange	p
Mortar-element	Skew-symmetric	Baseline	Lagrange	$p+1$
Mortar-element	Skew-symmetric	Modified	Lagrange	$p+1$
Global SBP-operator	Divergence	Global	Lagrange	p
Global SBP-operator	Divergence	Global	Lagrange	$p+1$
Global SBP-operator	Skew-symmetric	Global	Lagrange	p
Global SBP-operator	Skew-symmetric	Global	Lagrange	$p+1$

in Table 2, the six accuracy measures outlined in Table 1 were evaluated for degree one through four LGL and LG operators. With respect to accuracy, it was found that the the mortar-element divergence and skew-symmetric discretizations give similar results, likewise for the global SBP-operator divergence and skew-symmetric discretizations. Therefore, the presentation of the results is restricted to the divergence forms of the schemes with the understanding that the same conclusions apply to the skew-symmetric forms. Furthermore, in the tables that follow the data are only shown for the degree two and three operators (one even degree operator and one odd degree operator) for conciseness.

Table 3 gives the accuracy results when using the mortar-element discretization of the divergence form of the linear convection equation using the baseline approach for the metrics with a degree p Lagrange mapping in each element. All operator types and degrees converge at either optimal or near optimal rates with respect to both primal and dual truncation, solution, and functional error. Relative to the LGL operators, the discretizations based on LG operators generally have similar convergence rates with lower error values. Note that in this case, the baseline and modified approaches for the metrics

Table 3: Numerical results for the mortar-element discretization of the divergence form of the linear convection equation using the baseline approach for the metrics with a degree p Lagrange mapping in each element. Convergence rates based on the three finest grids.

			Primal error			Dual error		
Operator	p	**Element size**	**Truncation**	**Solution**	**Functional**	**Truncation**	**Solution**	**Functional**
LGL	2	5.00e−01	1.39e+01	2.80e−01	2.81e−01	3.68e+00	2.03e−01	2.81e−01
		2.50e−01	6.34e+00	8.37e−02	2.05e−02	1.11e+00	5.09e−02	2.05e−02
		1.25e−01	1.46e+00	1.08e−02	8.74e−04	3.78e−01	7.15e−03	8.74e−04
		6.25e−02	3.65e−01	1.36e−03	2.82e−05	1.06e−01	8.87e−04	2.82e−05
Convergence rate			2.06	2.97	4.75	1.70	2.92	4.75
LGL	3	5.00e−01	8.76e+00	1.37e−01	7.88e−02	1.51e+00	8.43e−02	7.88e−02
		2.50e−01	9.65e−01	8.90e−03	4.62e−04	4.14e−01	7.21e−03	4.62e−04
		1.25e−01	1.56e−01	7.15e−04	2.10e−06	4.40e−02	3.76e−04	2.10e−06
		6.25e−02	1.87e−02	4.39e−05	7.90e−09	6.26e−03	2.31e−05	7.90e−09
Convergence rate			2.84	3.83	7.92	3.02	4.14	7.92
LG	2	5.00e−01	5.25e+00	7.16e−02	1.01e−02	2.21e+00	4.85e−02	1.01e−02
		2.50e−01	1.89e+00	1.41e−02	3.49e−03	6.86e−01	9.98e−03	3.49e−03
		1.25e−01	5.51e−01	1.95e−03	1.42e−04	2.05e−01	1.42e−03	1.42e−04
		6.25e−02	1.49e−01	2.41e−04	4.61e−06	5.54e−02	1.75e−04	4.61e−06
Convergence rate			1.83	2.93	4.78	1.82	2.92	4.78
LG	3	5.00e−01	2.80e+00	2.75e−02	1.02e−02	1.04e+00	1.93e−02	1.02e−02
		2.50e−01	6.64e−01	2.10e−03	1.10e−04	2.61e−01	1.67e−03	1.10e−04
		1.25e−01	7.49e−02	1.10e−04	6.69e−07	2.96e−02	8.38e−05	6.69e−07
		6.25e−02	1.08e−02	6.86e−06	5.44e−09	4.34e−03	5.17e−06	5.44e−09
Convergence rate			2.97	4.13	7.16	2.95	4.17	7.16

return identical results when using degree p mappings and this is why only the results using the baseline approach for the metrics are given.

Table 4 gives the accuracy results when using the mortar-element discretization of the divergence form of the linear convection equation using the baseline approach for the metrics with a degree $p+1$ Lagrange mapping in each element. Although this specific problem does not require the use of a degree $p+1$ mapping, when solving more complex nonlinear problems the use of higher degree mappings can be beneficial (see, for example, [1,35]), which motivates the study of the use of higher degree mappings in the present linear context. From Table 4, the results with the LGL operators are virtually indistinguishable from the degree p mapping results summarized in Table 3. Likewise, the primal and dual truncation and solution error values and convergence rates with the LG operators with the degree $p+1$ mappings are very similar to those with the degree p mappings. In contrast, the functional convergence rates with the LG operators are significantly reduced with the baseline approach for the metrics relative to the LGL operators and relative to the LG operators with the degree p mappings, due to the degree p accuracy of the LG extrapolation operators. Note that because the dual truncation error still converges at a rate close to p, this indicates that this loss of functional superconvergence is not due to a lack of dual consistency.

Table 5 gives the accuracy results when using the mortar-element discretization of the divergence form of the linear convection equation using the

Table 4: Numerical results for the mortar-element discretization of the divergence form of the linear convection equation using the baseline approach for the metrics with a degree $p+1$ Lagrange mapping in each element. Convergence rates based on the three finest grids.

			Primal error			Dual error		
Operator	p	**Element size**	**Truncation**	**Solution**	**Functional**	**Truncation**	**Solution**	**Functional**
LGL	2	5.00e−01	1.35e+01	2.78e−01	2.78e−01	3.57e+00	2.00e−01	2.78e−01
		2.50e−01	6.32e+00	8.36e−02	2.05e−02	1.11e+00	5.09e−02	2.05e−02
		1.25e−01	1.46e+00	1.08e−02	8.74e−04	3.78e−01	7.15e−03	8.74e−04
		6.25e−02	3.65e−01	1.36e−03	2.82e−05	1.06e−01	8.87e−04	2.82e−05
Convergence rate			2.06	2.97	4.75	1.69	2.92	4.75
LGL	3	5.00e−01	8.56e+00	1.36e−01	7.92e−02	1.51e+00	8.43e−02	7.92e−02
		2.50e−01	9.65e−01	8.89e−03	4.60e−04	4.13e−01	7.19e−03	4.60e−04
		1.25e−01	1.55e−01	7.15e−04	2.10e−06	4.40e−02	3.76e−04	2.10e−06
		6.25e−02	1.87e−02	4.38e−05	7.89e−09	6.26e−03	2.31e−05	7.89e−09
Convergence rate			2.84	3.83	7.92	3.02	4.14	7.92
LG	2	5.00e−01	5.18e+00	7.06e−02	1.12e−02	2.15e+00	4.76e−02	1.12e−02
		2.50e−01	1.88e+00	1.48e−02	1.15e−02	8.62e−01	1.06e−02	1.15e−02
		1.25e−01	5.49e−01	2.38e−03	2.93e−03	3.02e−01	1.59e−03	2.93e−03
		6.25e−02	1.47e−01	4.43e−04	7.56e−04	7.81e−02	2.44e−04	7.56e−04
Convergence rate			1.84	2.53	1.97	1.73	2.72	1.97
LG	3	5.00e−01	2.86e+00	2.94e−02	2.93e−02	1.43e+00	2.04e−02	2.93e−02
		2.50e−01	6.64e−01	2.14e−03	1.02e−03	2.61e−01	1.75e−03	1.02e−03
		1.25e−01	7.56e−02	1.15e−04	6.57e−05	2.99e−02	8.58e−05	6.57e−05
		6.25e−02	1.09e−02	7.16e−06	4.20e−06	4.25e−03	5.26e−06	4.20e−06
Convergence rate			2.97	4.11	3.96	2.97	4.19	3.96

modified approach for the metrics with a degree $p+1$ Lagrange mapping in each element. With respect to the present accuracy measures being studied, the main benefit of the modified approach for the metrics is the retention of functional superconvergence with LG operators when using degree $p+1$ mappings. In [7], the lack of conservation with the LG discretizations with the baseline approach for the metrics in three dimensions was highlighted as one of the motivating factors for using the modified approach for the metrics. From the present numerical results, it is observed that considerations of functional accuracy also provide strong motivation for using the modified approach for the metrics for LG discretizations.

Tables 6 and 7 give the accuracy results when using the global SBP-operator discretization of the divergence form of the linear convection equation using the global approach for the metrics with degree p and $p+1$ Lagrange mappings in each element, respectively. With degree p mappings, approximately optimal truncation and solution error convergences rates are observed, along with functional superconvergence for both the LGL and LG families of operators. With degree $p+1$ mappings, functional superconvergence is observed for the LGL schemes and suboptimal functional convergence is observed for the LG schemes (a similar trend is observed when using exact mappings), despite the dual truncation error converging close to order p. Therefore, functional accuracy could be considered as a criterion for potentially preferring the mortar-element approach over the global SBP-operator approach.

Table 5: Numerical results for the mortar-element discretization of the divergence form of the linear convection equation using the modified approach for the metrics with a degree $p+1$ Lagrange mapping in each element. Convergence rates based on the three finest grids.

			Primal error			Dual error		
Operator	p	**Element size**	**Truncation**	**Solution**	**Functional**	**Truncation**	**Solution**	**Functional**
LGL	2	5.00e−01	1.35e+01	2.78e−01	2.78e−01	3.57e+00	2.00e−01	2.78e−01
		2.50e−01	5.90e+00	8.43e−02	2.97e−02	1.20e+00	5.19e−02	2.97e−02
		1.25e−01	1.53e+00	1.09e−02	1.60e−03	4.21e−01	7.27e−03	1.60e−03
		6.25e−02	3.77e−01	1.37e−03	7.42e−05	1.17e−01	9.06e−04	7.42e−05
Convergence rate			1.98	2.97	4.32	1.68	2.92	4.32
LGL	3	5.00e−01	8.27e+00	1.39e−01	6.91e−02	1.89e+00	8.56e−02	6.91e−02
		2.50e−01	9.69e−01	9.06e−03	5.11e−04	4.04e−01	7.37e−03	5.11e−04
		1.25e−01	1.58e−01	7.21e−04	2.56e−06	4.52e−02	3.85e−04	2.56e−06
		6.25e−02	1.90e−02	4.43e−05	1.41e−08	6.49e−03	2.37e−05	1.41e−08
Convergence rate			2.84	3.84	7.57	2.98	4.14	7.57
LG	2	5.00e−01	5.17e+00	7.06e−02	1.12e−02	2.15e+00	4.76e−02	1.12e−02
		2.50e−01	1.89e+00	1.43e−02	3.60e−03	7.13e−01	1.03e−02	3.60e−03
		1.25e−01	5.90e−01	1.99e−03	1.51e−04	2.25e−01	1.46e−03	1.51e−04
		6.25e−02	1.61e−01	2.46e−04	4.88e−06	6.03e−02	1.79e−04	4.88e−06
Convergence rate			1.78	2.93	4.76	1.78	2.92	4.76
LG	3	5.00e−01	3.04e+00	2.88e−02	1.07e−02	1.21e+00	2.06e−02	1.07e−02
		2.50e−01	6.69e−01	2.16e−03	1.20e−04	2.60e−01	1.72e−03	1.20e−04
		1.25e−01	7.39e−02	1.13e−04	7.13e−07	2.99e−02	8.59e−05	7.13e−07
		6.25e−02	1.09e−02	6.99e−06	5.78e−09	4.34e−03	5.29e−06	5.78e−09
Convergence rate			2.97	4.13	7.17	2.95	4.17	7.17

Table 6: Numerical results for the global SBP-operator discretization of the divergence form of the linear convection equation using the global approach for the metrics with a degree p Lagrange mapping in each element. Convergence rates based on the three finest grids.

			Primal error			Dual error		
Operator	p	**Element size**	**Truncation**	**Solution**	**Functional**	**Truncation**	**Solution**	**Functional**
LGL	2	5.00e−01	1.39e+01	2.80e−01	2.81e−01	3.68e+00	2.03e−01	2.81e−01
		2.50e−01	6.34e+00	8.37e−02	2.05e−02	1.11e+00	5.09e−02	2.05e−02
		1.25e−01	1.46e+00	1.08e−02	8.74e−04	3.78e−01	7.15e−03	8.74e−04
		6.25e−02	3.65e−01	1.36e−03	2.82e−05	1.06e−01	8.87e−04	2.82e−05
Convergence rate			2.06	2.97	4.75	1.70	2.92	4.75
LGL	3	5.00e−01	8.76e+00	1.37e−01	7.88e−02	1.51e+00	8.43e−02	7.88e−02
		2.50e−01	9.65e−01	8.90e−03	4.62e−04	4.14e−01	7.21e−03	4.62e−04
		1.25e−01	1.56e−01	7.15e−04	2.10e−06	4.40e−02	3.76e−04	2.10e−06
		6.25e−02	1.87e−02	4.39e−05	7.90e−09	6.26e−03	2.31e−05	7.90e−09
Convergence rate			2.84	3.83	7.92	3.02	4.14	7.92
LG	2	5.00e−01	5.86e+00	7.12e−02	1.74e−02	2.21e+00	4.83e−02	1.74e−02
		2.50e−01	2.21e+00	1.73e−02	3.43e−03	6.85e−01	1.01e−02	3.43e−03
		1.25e−01	7.06e−01	2.15e−03	1.42e−04	2.08e−01	1.40e−03	1.42e−04
		6.25e−02	1.83e−01	2.66e−04	4.61e−06	5.52e−02	1.74e−04	4.61e−06
Convergence rate			1.80	3.01	4.77	1.82	2.93	4.77
LG	3	5.00e−01	3.74e+00	3.48e−02	9.73e−03	1.04e+00	2.03e−02	9.73e−03
		2.50e−01	7.25e−01	2.25e−03	1.06e−04	2.61e−01	1.59e−03	1.06e−04
		1.25e−01	9.58e−02	1.59e−04	6.55e−07	2.96e−02	8.28e−05	6.55e−07
		6.25e−02	1.27e−02	9.84e−06	5.40e−09	4.34e−03	5.16e−06	5.40e−09
Convergence rate			2.92	3.92	7.13	2.96	4.14	7.13

Table 7: Numerical results for the global SBP-operator discretization of the divergence form of the linear convection equation using the global approach for the metrics with a degree $p+1$ Lagrange mapping in each element. Convergence rates based on the three finest grids.

			Primal error			Dual error		
Operator	p	**Element size**	**Truncation**	**Solution**	**Functional**	**Truncation**	**Solution**	**Functional**
LGL	2	5.00e−01	1.35e+01	2.78e−01	2.78e−01	3.57e+00	2.00e−01	2.78e−01
		2.50e−01	6.32e+00	8.36e−02	2.05e−02	1.11e+00	5.09e−02	2.05e−02
		1.25e−01	1.46e+00	1.08e−02	8.74e−04	3.78e−01	7.15e−03	8.74e−04
		6.25e−02	3.65e−01	1.36e−03	2.82e−05	1.06e−01	8.87e−04	2.82e−05
Convergence rate			2.06	2.97	4.75	1.69	2.92	4.75
LGL	3	5.00e−01	8.56e+00	1.36e−01	7.92e−02	1.51e+00	8.43e−02	7.92e−02
		2.50e−01	9.65e−01	8.89e−03	4.60e−04	4.13e−01	7.19e−03	4.60e−04
		1.25e−01	1.55e−01	7.15e−04	2.10e−06	4.40e−02	3.76e−04	2.10e−06
		6.25e−02	1.87e−02	4.38e−05	7.89e−09	6.26e−03	2.31e−05	7.89e−09
Convergence rate			2.84	3.83	7.92	3.02	4.14	7.92
LG	2	5.00e−01	5.65e+00	7.01e−02	1.77e−02	2.15e+00	4.74e−02	1.77e−02
		2.50e−01	2.21e+00	1.80e−02	7.36e−03	7.14e−01	1.04e−02	7.36e−03
		1.25e−01	7.39e−01	2.28e−03	8.25e−04	2.27e−01	1.45e−03	8.25e−04
		6.25e−02	1.95e−01	2.83e−04	9.61e−05	5.92e−02	1.81e−04	9.61e−05
Convergence rate			1.75	3.00	3.13	1.80	2.92	3.13
LG	3	5.00e−01	3.88e+00	3.79e−02	1.91e−02	1.17e+00	2.16e−02	1.91e−02
		2.50e−01	7.27e−01	2.28e−03	5.72e−04	2.62e−01	1.63e−03	5.72e−04
		1.25e−01	9.89e−02	1.61e−04	1.66e−05	2.97e−02	8.32e−05	1.66e−05
		6.25e−02	1.27e−02	9.87e−06	5.15e−07	4.32e−03	5.16e−06	5.15e−07
Convergence rate			2.92	3.93	5.06	2.96	4.15	5.06

5 Accurate solutions and functionals for the Euler equations

In this section a dual-consistent mortar-element discretization of the Euler equations is presented that is based on the divergence form of the governing equations. In the context of the Euler equations, it will be seen that the use of degree $p+1$ mappings facilitates the accuracy of the flow tangency boundary condition. Hence, the mortar-element approach is preferred over the global SBP-operator approach due to the ability of the mortar-element approach to retain functional superconvergence in the presence of degree $p+1$ mappings when using LG operators. Furthermore, in the context of the linear convection equation the divergence and skew-symmetric discretizations gave very similar results in terms of accuracy. Therefore, in this section only the discretization of the divergence form is presented for simplicity, and also because the divergence form of the governing equations is used for simulating many practical problems [15, 26].

Table 8: Components of the outward unit normal, $\boldsymbol{n} = n_{\xi_1}\,\hat{\boldsymbol{\xi}}_1 + n_{\xi_2}\,\hat{\boldsymbol{\xi}}_2 = n_{x_1}\,\hat{\mathbf{x}}_1 + n_{x_2}\,\hat{\mathbf{x}}_2$, on each side of $\hat{\Omega}$. The face numbering convention is the same as that outlined in Table 1 in [7].

Face number	n_{ξ_1}	n_{ξ_2}	n_{x_1}	n_{x_2}
1	-1	0	$-\frac{\partial\xi_1}{\partial x_1} / \|\nabla\xi_1\|$	$-\frac{\partial\xi_1}{\partial x_2} / \|\nabla\xi_1\|$
2	1	0	$\frac{\partial\xi_1}{\partial x_1} / \|\nabla\xi_1\|$	$\frac{\partial\xi_1}{\partial x_2} / \|\nabla\xi_1\|$
3	0	-1	$-\frac{\partial\xi_2}{\partial x_1} / \|\nabla\xi_2\|$	$-\frac{\partial\xi_2}{\partial x_2} / \|\nabla\xi_2\|$
4	0	1	$\frac{\partial\xi_2}{\partial x_1} / \|\nabla\xi_2\|$	$\frac{\partial\xi_2}{\partial x_2} / \|\nabla\xi_2\|$

5.1 Two-dimensional Euler equations

On a single element, the transformed steady two-dimensional compressible Euler equations are given by

$$\nabla\cdot\boldsymbol{\mathcal{F}} \coloneqq \sum_{l=1}^{2}\frac{\partial}{\partial\xi_l}\left(\sum_{m=1}^{2}\mathcal{J}\frac{\partial\xi_l}{\partial x_m}\boldsymbol{\mathcal{F}}_{x_m}(\boldsymbol{\mathcal{U}})\right) = \mathbf{0} \quad \text{in } \hat{\Omega}, \tag{26}$$

where definitions of the vector of conservative variables $\boldsymbol{\mathcal{U}}$ and the flux vectors $\boldsymbol{\mathcal{F}}_{x_m}$ can be found in [28], for example. To complete the description of the continuous primal problem, (26) is supplemented with appropriate boundary conditions. For example, suppose the reference domain includes a wall boundary, $\hat{\Gamma}_{\mathrm{W}}$, and a farfield boundary, $\hat{\Gamma}\setminus\hat{\Gamma}_{\mathrm{W}}$. On the wall boundary, the normal flux is constrained as follows

$$\boldsymbol{n}\cdot\boldsymbol{\mathcal{F}} = \sum_{l=1}^{2} n_{\xi_l}\boldsymbol{\mathcal{F}}_{\xi_l}(\mathsf{P}\boldsymbol{\mathcal{U}}) \quad \text{on } \hat{\Gamma}_{\mathrm{W}}, \tag{27}$$

which enforces flow tangency by using the matrix P to remove the normal component of momentum from $\boldsymbol{\mathcal{U}}$, where

$$\boldsymbol{\mathcal{F}}_{\xi_l} \coloneqq \sum_{m=1}^{2}\mathcal{J}\frac{\partial\xi_l}{\partial x_m}\boldsymbol{\mathcal{F}}_{x_m} \quad \text{and} \quad \mathsf{P} \coloneqq \begin{bmatrix} 1 & 0 & 0 & 0 \\ 0 & 1-n_{x_1}^2 & -n_{x_1}n_{x_2} & 0 \\ 0 & -n_{x_2}n_{x_1} & 1-n_{x_2}^2 & 0 \\ 0 & 0 & 0 & 1 \end{bmatrix}. \tag{28}$$

Here, n_{x_1} and n_{x_2} are components of $\boldsymbol{n} = n_{x_1}\,\hat{\mathbf{x}}_1 + n_{x_2}\,\hat{\mathbf{x}}_2$, where $\boldsymbol{n}$ is the outward unit normal vector and $\hat{\mathbf{x}}_1$ and $\hat{\mathbf{x}}_2$ are unit coordinate vectors. For reference, the different components of the outward unit normal on each side of $\hat{\Omega}$ are given in Table 8.

On the farfield boundary, the following condition is specified

$$\boldsymbol{n}\cdot\boldsymbol{\mathcal{F}} = \mathsf{A}^{+}\boldsymbol{\mathcal{U}} + \mathsf{A}^{-}\boldsymbol{\mathcal{U}}_{\infty} \quad \text{on } \hat{\Gamma}\setminus\hat{\Gamma}_{\mathrm{W}}, \tag{29}$$

where $\boldsymbol{\mathcal{U}}_{\infty}$ is the farfield state and $\mathsf{A}^{\pm} = \mathsf{A}^{\pm}(\boldsymbol{\mathcal{U}}, \boldsymbol{n})$ with

$$\mathsf{A}^{\pm} \coloneqq \frac{1}{2}\left(\mathsf{A} \pm |\mathsf{A}|\right) \quad \text{and} \quad \mathsf{A} \coloneqq \sum_{l=1}^{2}\mathsf{A}_{\xi_l}n_{\xi_l}, \tag{30}$$

where

$$\mathsf{A}_{\xi_l} \coloneqq \sum_{m=1}^{2} \mathcal{J} \frac{\partial \xi_l}{\partial x_m} \mathsf{A}_{x_m} \quad \text{and} \quad \mathsf{A}_{x_m} \coloneqq \frac{\partial \boldsymbol{\mathcal{F}}_{x_m}}{\partial \boldsymbol{\mathcal{U}}}. \tag{31}$$

The matrix A can be diagonalized as follows

$$\mathsf{A} = \mathsf{X}\Lambda\mathsf{X}^{-1},$$

where X and X^{-1} are matrices holding the right and left eigenvectors of A, respectively, and Λ is a diagonal matrix holding the eigenvalues of A (see [14] for more details). To obtain $|\mathsf{A}|$, the eigenvalues of A contained along the diagonal of the matrix Λ are replaced with their absolute values.

5.2 Corresponding continuous dual equations

To derive the continuous dual problem corresponding to (26), it is helpful to introduce the following boundary force functional

$$\mathcal{I}(\boldsymbol{\mathcal{U}}) \coloneqq \int_{\hat{\Gamma}} i(\boldsymbol{\mathcal{U}})\, d\hat{\Gamma} = \int_{\hat{\Gamma}_{\mathrm{W}}} \breve{\boldsymbol{\phi}}^{\mathrm{T}} \left\{ \boldsymbol{n} \cdot \boldsymbol{\mathcal{F}}(\mathsf{P}\boldsymbol{\mathcal{U}}) \right\} d\hat{\Gamma}, \tag{32}$$

where $i(\boldsymbol{\mathcal{U}}) \coloneqq \breve{\boldsymbol{\phi}}^{\mathrm{T}} \left\{ \boldsymbol{n} \cdot \boldsymbol{\mathcal{F}}(\mathsf{P}\boldsymbol{\mathcal{U}}) \right\}$ on $\hat{\Gamma}_{\mathrm{W}}$ and $i(\boldsymbol{\mathcal{U}}) \coloneqq 0$ on $\hat{\Gamma} \setminus \hat{\Gamma}_{\mathrm{W}}$, and, following Hartmann and Leicht [14], for example, the vector $\breve{\boldsymbol{\phi}}$ is defined by

$$\breve{\boldsymbol{\phi}} \coloneqq \begin{bmatrix} 0 & \boldsymbol{\phi}^{\mathrm{T}} & 0 \end{bmatrix}^{\mathrm{T}} \tag{33}$$

with

$$\boldsymbol{\phi} = \begin{cases} (\cos(\alpha), \sin(\alpha))^{\mathrm{T}} & \text{for drag} \\ (-\sin(\alpha), \cos(\alpha))^{\mathrm{T}} & \text{for lift,} \end{cases} \tag{34}$$

where α is the angle of attack. The corresponding strong form of the dual problem is given by

$$-\left(\boldsymbol{\mathcal{F}}'[\boldsymbol{\mathcal{U}}]\right)^{\mathrm{T}} \nabla \boldsymbol{\psi} = \boldsymbol{0} \quad \text{in } \hat{\Omega}, \qquad \left(\boldsymbol{n} \cdot \boldsymbol{\mathcal{F}}'[\boldsymbol{\mathcal{U}}]\right)^{\mathrm{T}} \boldsymbol{\psi} = \left(i'[\boldsymbol{\mathcal{U}}]\right)^{\mathrm{T}} \quad \text{on } \hat{\Gamma}. \tag{35}$$

On the wall boundary the following term is obtained:

$$\begin{aligned} \boldsymbol{n} \cdot \boldsymbol{\mathcal{F}} &= \sum_{l=1}^{2} n_{\xi_l} \mathcal{F}_{\xi_l}(\mathsf{P}\mathcal{U}) = \sum_{l=1}^{2} n_{\xi_l} \left[0 \;\; \mathcal{J} \tfrac{\partial \xi_l}{\partial x_1} p \;\; \mathcal{J} \tfrac{\partial \xi_l}{\partial x_2} p \;\; 0 \right]^{\mathrm{T}} \times \frac{\|\nabla \xi_l\|}{\|\nabla \xi_l\|} \\ &= \sum_{l=1}^{2} \mathcal{J} \|\nabla \xi_l\| \breve{\boldsymbol{n}} p, \text{ where } \breve{\boldsymbol{n}} = \begin{bmatrix} 0 & \boldsymbol{n}^{\mathrm{T}} & 0 \end{bmatrix}^{\mathrm{T}}. \end{aligned}$$

Also, expanding $i(\boldsymbol{\mathcal{U}})$ along $\hat{\Gamma}_{\mathrm{W}}$ gives

$$i(\boldsymbol{\mathcal{U}}) = \breve{\boldsymbol{\phi}}^{\mathrm{T}} \left\{ \sum_{l=1}^{2} n_{\xi_l} \mathcal{F}_{\xi_l}(\mathsf{P}\mathcal{U}) \right\} = \sum_{l=1}^{2} \mathcal{J} \|\nabla \xi_l\| \breve{\boldsymbol{\phi}}^{\mathrm{T}} \breve{\boldsymbol{n}} p.$$

Then, expanding $\left(\boldsymbol{n}\cdot\boldsymbol{\mathcal{F}}'[\boldsymbol{\mathcal{U}}]\right)^{\mathrm{T}}\boldsymbol{\psi} = \left(i'[\boldsymbol{\mathcal{U}}]\right)^{\mathrm{T}}$ from (35), along $\hat{\Gamma}_{\mathrm{W}}$, gives

$$\sum_{l=1}^{2}\mathcal{J}\left\|\nabla\xi_l\right\|\left(p'[\boldsymbol{\mathcal{U}}]\right)^{\mathrm{T}}\breve{\boldsymbol{n}}^{\mathrm{T}}\boldsymbol{\psi} = \sum_{l=1}^{2}\mathcal{J}\left\|\nabla\xi_l\right\|\left(p'[\boldsymbol{\mathcal{U}}]\right)^{\mathrm{T}}\breve{\boldsymbol{n}}^{\mathrm{T}}\breve{\boldsymbol{\phi}}, \tag{36}$$

where $p'[\boldsymbol{\mathcal{U}}]\in\mathbb{R}^{1\times 4}$. This implies that the dual boundary condition along $\hat{\Gamma}_{\mathrm{W}}$ is given by

$$\breve{\boldsymbol{n}}^{\mathrm{T}}\boldsymbol{\psi} = \breve{\boldsymbol{n}}^{\mathrm{T}}\breve{\boldsymbol{\phi}} \quad \text{on } \hat{\Gamma}_{\mathrm{W}}. \tag{37}$$

On the farfield boundary the following term is obtained:

$$\left(\boldsymbol{n}\cdot\boldsymbol{\mathcal{F}}'[\boldsymbol{\mathcal{U}}]\right)^{\mathrm{T}}\boldsymbol{\psi} = \boldsymbol{0} \quad \text{on } \hat{\Gamma}\setminus\hat{\Gamma}_{\mathrm{W}}. \tag{38}$$

Similar results may be found in [13,18,14].

5.3 Discretization of the two-dimensional Euler equations

The divergence form of the Euler equations given by (26) is discretized using the mortar-element approach. This gives on a single element

$$\sum_{l,m=1}^{2}\mathsf{D}_{\xi_l}\operatorname{diag}\left(\widetilde{\mathcal{J}\frac{\partial\xi_l}{\partial x_m}}\right)_h\boldsymbol{f}_{x_m}(\boldsymbol{u}_h) = \mathrm{SAT}^{\boldsymbol{u}_h}_{(2l-1)} + \mathrm{SAT}^{\boldsymbol{u}_h}_{(2l)}, \tag{39}$$

where the boundary SAT on the $2l-1$ face, for example, is defined by

$$\mathrm{SAT}^{\boldsymbol{u}_h}_{(2l-1)} \coloneqq \mathsf{H}^{-1}\sum_{l=1}^{2}\left\{-\mathsf{R}^{\mathrm{T}}_{\alpha_{\xi_l}}\mathsf{H}^{\perp}_{\xi_l}\left(\boldsymbol{f}_{(2l-1),h}(\boldsymbol{u}_h) - \boldsymbol{f}^{\star}_{(2l-1),h}(\boldsymbol{u}_h)\right)\right\},$$

where

$$\boldsymbol{f}_{(2l-1),h}(\boldsymbol{u}_h) \coloneqq \sum_{m=1}^{2}\mathsf{R}_{\alpha_{\xi_l}}\operatorname{diag}\left(\widetilde{\mathcal{J}\frac{\partial\xi_l}{\partial x_m}}\right)_h\boldsymbol{f}_{x_m}(\boldsymbol{u}_h).$$

The following notation has been introduced for the volume metric terms

$$\operatorname{diag}\left(\widetilde{\mathcal{J}\frac{\partial\xi_l}{\partial x_m}}\right)_h \coloneqq \operatorname{diag}\left(\mathcal{J}\frac{\partial\xi_l}{\partial x_m}\right)_h\otimes\mathsf{I}_4,$$

with analogous notation being adopted for the surface metric terms. The numerical fluxes in the SATs depend on the boundary conditions being applied. As in [18], suppose that farfield boundary conditions are specified on faces 1, 2, and 4, and a wall boundary condition is specified on face 3. In this case, the numerical boundary flux functions on faces 3 and 4, for example, are given by

$$\begin{aligned}
\boldsymbol{f}^{\star}_{(3),h}(\boldsymbol{u}_h) &\coloneqq \sum_{m=1}^{2}\operatorname{diag}\left(\widetilde{\mathcal{J}\frac{\partial\xi_2}{\partial x_m}}\right)^{[3]}_h\boldsymbol{f}_{x_m}(\tilde{\mathsf{P}}_h\mathsf{R}_{\alpha_{\xi_2}}\boldsymbol{u}_h) \text{ and}\\
\boldsymbol{f}^{\star}_{(4),h}(\boldsymbol{u}_h) &\coloneqq \mathsf{A}^{+}_{(4),h}(\boldsymbol{u}_h)\,\mathsf{R}_{\beta_{\xi_2}}\boldsymbol{u}_h + \mathsf{A}^{-}_{(4),h}(\boldsymbol{u}_h)\times(\mathbf{1}_{\xi_1}\otimes\boldsymbol{\mathcal{U}}_{\infty}),
\end{aligned}$$

where $\tilde{\mathsf{P}}_h = \mathsf{I}_{\xi_1} \otimes \mathsf{I}_4 - \tilde{\boldsymbol{n}}_h \tilde{\boldsymbol{n}}_h^{\mathrm{T}} \in \mathbb{R}^{4N_{\xi_1} \times 4N_{\xi_1}}$ with

$$\tilde{\boldsymbol{n}}_h = \begin{bmatrix} \breve{\boldsymbol{n}}_h(\xi_{1,1}, \xi_{2,\alpha_{\xi_2}}) & & & \\ & \breve{\boldsymbol{n}}_h(\xi_{1,2}, \xi_{2,\alpha_{\xi_2}}) & & \\ & & \ddots & \\ & & & \breve{\boldsymbol{n}}_h(\xi_{1,N_{\xi_1}}, \xi_{2,\alpha_{\xi_2}}) \end{bmatrix} \in \mathbb{R}^{4N_{\xi_1} \times N_{\xi_1}}$$

and

$$\breve{\boldsymbol{n}}_h(\xi_1, \xi_2) = \begin{bmatrix} 0 & n_{x_1,h}(\xi_1, \xi_2) & n_{x_2,h}(\xi_1, \xi_2) & 0 \end{bmatrix}^{\mathrm{T}}.$$

The boundary flux Jacobian terms in $\boldsymbol{f}^{\star}_{(4),h}$, for example, are computed from

$$\mathsf{A}_{(4),h}(\boldsymbol{u}_h) = \sum_{m=1}^{2} \operatorname{diag}\left(\widetilde{\mathcal{J} \frac{\partial \xi_2}{\partial x_m}} \right)_h^{[4]} \mathsf{A}_{x_m}(\mathsf{R}_{\beta_{\xi_2}} \boldsymbol{u}_h),$$

where $\mathsf{A}_{x_m}(\boldsymbol{u}) = \partial \boldsymbol{f}_{x_m}(\boldsymbol{u}) / \partial \boldsymbol{u}$, $m = 1, 2$, are block diagonal matrices.

The discrete integral functional is given by

$$\mathcal{I}_h(\boldsymbol{u}_h) \coloneqq -(\mathbf{1}_{\xi_1} \otimes \mathbf{1}_{\xi_2} \otimes \breve{\boldsymbol{\phi}})^{\mathrm{T}} \mathsf{R}_{\alpha_{\xi_2}}^{\mathrm{T}} \mathsf{H}_{\xi_2}^{\perp} \boldsymbol{f}^{\star}_{(3),h}(\boldsymbol{u}_h). \tag{40}$$

This leads to the following discrete dual problem

$$\begin{gathered} -\sum_{l,m=1}^{2} \left\{ \operatorname{diag}\left(\mathcal{J} \frac{\partial \xi_l}{\partial x_m} \right)_h \boldsymbol{f}'_{x_m}[\boldsymbol{u}_h] \right\}^{\mathrm{T}} \mathsf{D}_{\xi_l} \boldsymbol{\psi}_h = \\ \operatorname{diag}(\mathcal{J}_h)\, \boldsymbol{g} + \mathrm{SAT}^{\boldsymbol{\psi}_h}_{(2l-1)} + \mathrm{SAT}^{\boldsymbol{\psi}_h}_{(2l)}, \end{gathered} \tag{41}$$

where the boundary SAT on the $2l-1$ face, for example, is given by

$$\begin{aligned} \mathrm{SAT}^{\boldsymbol{\psi}_h}_{(2l-1)} \coloneqq{}& \mathsf{H}^{-1} \sum_{l=1}^{2} \left\{ \boldsymbol{f}^{\star\prime}_{(2l-1),h}[\boldsymbol{u}_h] \right\}^{\mathrm{T}} \mathsf{H}_{\xi_l}^{\perp} \mathsf{R}_{\alpha_{\xi_l}} \boldsymbol{\psi}_h \\ & - \mathsf{H}^{-1} \left\{ \boldsymbol{f}^{\star\prime}_{(3),h}[\boldsymbol{u}_h] \right\}^{\mathrm{T}} \mathsf{H}_{\xi_2}^{\perp} \mathsf{R}_{\alpha_{\xi_2}} (\mathbf{1}_{\xi_1} \otimes \mathbf{1}_{\xi_2} \otimes \breve{\boldsymbol{\phi}}). \end{aligned}$$

5.4 Accuracy of the flow tangency boundary condition

Bassi and Rebay [1] were the first to recognize the importance of having high-order representations of curved boundaries in the presence of flow tangency boundary conditions. Subsequently, van der Vegt and van der Ven [31] showed that for the linear (i.e., $p = 1$) case the use of local mesh refinement provides another means of reducing the error associated with the boundary representation in conjunction with the flow tangency boundary condition in the context of the Euler equations. Furthermore, they showed that it is necessary to take the curved boundary into account for a consistent discontinuous Galerkin discretization [31]. Krivodonova and Berger [20] also proposed an alternative approach to recover accuracy in the presence of wall boundary

conditions without resorting to high order geometry representations. More recently, Zwanenburg and Nadarajah [35] compared the use of isoparametric and superparametric geometry representations. For the Euler equations, they observed suboptimal solution error convergence rates when using isoparametric geometry representations and optimal solution error convergence rates when using superparametric geometry representations [35]. Note that Bassi and Rebay [1] did not notice a similar benefit when using superparametric geometry representations with their degree $p = 2$ and degree $p = 3$ discretizations; however, Zwanenburg and Nadarajah [35] numerically demonstrated that this was likely because Bassi and Rebay only examined entropy error and used elements with aspect ratio close to one near wall boundaries [35]. Finally, Navah and Nadarajah [24] and Navah [23] found that using isoparametric geometry representations in combination with exact normals was sufficient to achieve good solution error convergence rates for a manufactured solution governed by the Euler equations.

The aim in this section is to provide a mathematical analysis of the accuracy of the flow tangency boundary condition to elucidate the reasons why superparametric geometry representations are beneficial when solving problems governed by the Euler equations (as observed by [1,31,35], for example). Furthermore, while this specific analysis is performed within the SBP framework, the conclusions could be extended to other types of discretization methodologies due to the generality of the SBP approach. To begin, consider the wall boundary SAT from the discretization of the Euler equations on a single element, given by

$$\begin{aligned}&\mathrm{SAT}^{\boldsymbol{u}}_{\mathrm{Wall}} \coloneqq -\mathsf{H}^{-1}\mathsf{R}^{\mathrm{T}}_{\alpha_{\xi_2}}\mathsf{H}^{\perp}_{\xi_2}\times\\ &\sum_{m=1}^{2}\left\{\mathsf{R}_{\alpha_{\xi_2}}\operatorname{diag}\left(\widetilde{\mathcal{J}\frac{\partial\xi_2}{\partial x_m}}\right)_h \boldsymbol{f}_{x_m}(\boldsymbol{u}) - \operatorname{diag}\left(\widetilde{\mathcal{J}\frac{\partial\xi_2}{\partial x_m}}\right)^{[3]}_h \boldsymbol{f}_{x_m}(\tilde{\mathsf{P}}_h\mathsf{R}_{\alpha_{\xi_2}}\boldsymbol{u})\right\},\end{aligned} \tag{42}$$

where $\boldsymbol{u}$ has been substituted for $\boldsymbol{u}_h$ because the objective is to show consistency. The wall boundary SAT, given by (42), is design order consistent for the Euler equations if

$$\left\|\operatorname{diag}\left(\mathcal{J}_h\right)^{-1}\mathrm{SAT}^{\boldsymbol{u}}_{\mathrm{Wall}}\right\|_{\infty} = \mathcal{O}(h^p), \tag{43}$$

since the Euler equations are a first-order system of PDEs. Note that the wall boundary SAT has been multiplied by $\operatorname{diag}\left(\mathcal{J}_h\right)^{-1}$ because the discretization is constructed in the computational domain and it is of interest to evaluate the consistency of the wall boundary SAT in the physical domain. The following theorem is now proven.

Theorem 1 *Assume that a degree p_g polynomial geometry representation is used in each element and assume that the wall normals are constructed directly from the degree p_g geometry representation. Then, assuming that the*

wall boundary SAT given by (42) is not trivially zero, the wall boundary SAT satisfies the consistency condition (43) if and only if $p_g \geq p+1$ (i.e., if and only if the geometry representation is superparametric, as opposed to being isoparametric or subparametric), where p_g and p are integers.

Proof Using the Cauchy-Schwarz inequality and noting that

$$\left\|\mathrm{diag}\left(\mathcal{J}_h\right)^{-1}\right\|_\infty = \mathcal{O}(h^{-2}), \quad \left\|\mathsf{H}^{-1}\right\|_\infty = \mathcal{O}(1),$$
$$\left\|\mathsf{R}_{\alpha_{\xi_2}}^{\mathrm{T}}\right\|_\infty = \mathcal{O}(1), \qquad \left\|\mathsf{H}_{\xi_2}^{\perp}\right\|_\infty = \mathcal{O}(1),$$

gives

$$\left\|\mathrm{diag}\left(\mathcal{J}_h\right)^{-1}\mathrm{SAT}_{\mathrm{Wall}}^{\boldsymbol{u}}\right\|_\infty = \mathcal{O}(h^{-2})\times$$
$$\left\|\sum_{m=1}^{2}\left\{\mathsf{R}_{\alpha_{\xi_2}}\,\mathrm{diag}\left(\widetilde{\mathcal{J}\frac{\partial\xi_2}{\partial x_m}}\right)_h \boldsymbol{f}_{x_m}(\boldsymbol{u}) - \mathrm{diag}\left(\widetilde{\mathcal{J}\frac{\partial\xi_2}{\partial x_m}}\right)_h^{[3]} \boldsymbol{f}_{x_m}(\tilde{\mathsf{P}}_h\mathsf{R}_{\alpha_{\xi_2}}\boldsymbol{u})\right\}\right\|_\infty .$$

Using the triangle inequality the summation can be brought outside the infinity norm to obtain

$$\left\|\mathrm{diag}\left(\mathcal{J}_h\right)^{-1}\mathrm{SAT}_{\mathrm{Wall}}^{\boldsymbol{u}}\right\|_\infty = \mathcal{O}(h^{-2})\times$$
$$\sum_{m=1}^{2}\left\|\mathsf{R}_{\alpha_{\xi_2}}\,\mathrm{diag}\left(\widetilde{\mathcal{J}\frac{\partial\xi_2}{\partial x_m}}\right)_h \boldsymbol{f}_{x_m}(\boldsymbol{u}) - \mathrm{diag}\left(\widetilde{\mathcal{J}\frac{\partial\xi_2}{\partial x_m}}\right)_h^{[3]} \boldsymbol{f}_{x_m}(\tilde{\mathsf{P}}_h\mathsf{R}_{\alpha_{\xi_2}}\boldsymbol{u})\right\|_\infty . \tag{44}$$

Due to the accuracy of $\mathsf{R}_{\alpha_{\xi_2}}$ and because $\mathrm{diag}\left(\widetilde{\mathcal{J}\frac{\partial\xi_2}{\partial x_m}}\right)_h = \mathcal{O}(h)$, the accuracy of the extrapolation of the flux multiplied by the volume metrics is given by

$$\mathsf{R}_{\alpha_{\xi_2}}\,\mathrm{diag}\left(\widetilde{\mathcal{J}\frac{\partial\xi_2}{\partial x_m}}\right)_h \boldsymbol{f}_{x_m}(\boldsymbol{u}) = \mathrm{diag}\left(\widetilde{\mathcal{J}\frac{\partial\xi_2}{\partial x_m}}\right)_h^{[3]} \boldsymbol{f}_{x_m}(\boldsymbol{u}_{[3]}) + \mathcal{O}(h^{r+2}), \tag{45}$$

where $r \geq p$ is the degree of the extrapolation operator $\mathsf{R}_{\alpha_{\xi_2}}$. Substituting (45) into (44), using the Cauchy-Schwarz inequality, and noting that

$$\left\|\mathrm{diag}\left(\widetilde{\mathcal{J}\frac{\partial\xi_2}{\partial x_m}}\right)_h^{[3]}\right\|_\infty = \mathcal{O}(h),$$

gives

$$\left\|\mathrm{diag}\left(\mathcal{J}_h\right)^{-1}\mathrm{SAT}_{\mathrm{Wall}}^{\boldsymbol{u}}\right\|_\infty = \mathcal{O}(h^{-1})\times$$
$$\sum_{m=1}^{2}\left\|\boldsymbol{f}_{x_m}(\boldsymbol{u}_{[3]}) - \boldsymbol{f}_{x_m}(\tilde{\mathsf{P}}_h\mathsf{R}_{\alpha_{\xi_2}}\boldsymbol{u}) + \mathcal{O}(h^{r+1})\right\|_\infty . \tag{46}$$

Now it is determined how well $\boldsymbol{f}_{x_m}(\tilde{\mathsf{P}}_h \mathsf{R}_{\alpha_{\xi_2}} \boldsymbol{u})$ approximates $\boldsymbol{f}_{x_m}(\tilde{\mathsf{P}}\boldsymbol{u}_{[3]})$, where $\tilde{\mathsf{P}}\boldsymbol{u}_{[3]} = \boldsymbol{u}_{[3]}$, since $\boldsymbol{u}_{[3]}$ is the exact solution on the wall boundary and therefore satisfies the wall boundary condition. As $\tilde{\mathsf{P}}_h = \mathsf{I}_{\xi_1} \otimes \mathsf{I}_4 - \tilde{\boldsymbol{n}}_h \tilde{\boldsymbol{n}}_h^{\mathrm{T}}$ depends on the wall normals, the accuracy of the wall normals is determined first. Recall from Table 8 that the components of the outward normals along side 3, which is the side corresponding to the wall boundary in this case, are given by

$$n_{x_1} = -\frac{\frac{\partial \xi_2}{\partial x_1}}{\sqrt{\left(\frac{\partial \xi_2}{\partial x_1}\right)^2 + \left(\frac{\partial \xi_2}{\partial x_2}\right)^2}} \quad \text{and} \quad n_{x_2} = -\frac{\frac{\partial \xi_2}{\partial x_2}}{\sqrt{\left(\frac{\partial \xi_2}{\partial x_1}\right)^2 + \left(\frac{\partial \xi_2}{\partial x_2}\right)^2}}.$$

Assuming the wall normals are constructed directly from a degree p_g geometry representation, at a given point along the wall boundary the following is obtained for $n_{x_1,h}$, for example,

$$n_{x_1,h} = -\frac{\left(\frac{\partial \xi_2}{\partial x_1}\right)_h}{\sqrt{\left(\left(\frac{\partial \xi_2}{\partial x_1}\right)_h\right)^2 + \left(\left(\frac{\partial \xi_2}{\partial x_2}\right)_h\right)^2}},$$

where

$$\left(\frac{\partial \xi_2}{\partial x_1}\right)_h = \frac{\partial \xi_2}{\partial x_1} + \mathcal{O}(h^{p_g-1}) \quad \text{and} \quad \left(\frac{\partial \xi_2}{\partial x_2}\right)_h = \frac{\partial \xi_2}{\partial x_2} + \mathcal{O}(h^{p_g-1}).$$

To determine the order of $n_{x_1} - n_{x_1,h}$, the following term is evaluated

$$\begin{aligned} &n_{x_1} - n_{x_1,h} \\ &= -\frac{\frac{\partial \xi_2}{\partial x_1}}{\sqrt{\left(\frac{\partial \xi_2}{\partial x_1}\right)^2 + \left(\frac{\partial \xi_2}{\partial x_2}\right)^2}} + \frac{\frac{\partial \xi_2}{\partial x_1} + \mathcal{O}(h^{p_g-1})}{\sqrt{\left(\frac{\partial \xi_2}{\partial x_1} + \mathcal{O}(h^{p_g-1})\right)^2 + \left(\frac{\partial \xi_2}{\partial x_2} + \mathcal{O}(h^{p_g-1})\right)^2}}, \end{aligned}$$

or, replacing $\mathcal{O}(h^{p_g-1})$ with ϵ in the second term on the right-hand side and performing a series expansion gives

$$\frac{\frac{\partial \xi_2}{\partial x_1} + \epsilon}{\sqrt{\left(\frac{\partial \xi_2}{\partial x_1} + \epsilon\right)^2 + \left(\frac{\partial \xi_2}{\partial x_2} + \epsilon\right)^2}} = \frac{\frac{\partial \xi_2}{\partial x_1}}{\sqrt{\left(\frac{\partial \xi_2}{\partial x_1}\right)^2 + \left(\frac{\partial \xi_2}{\partial x_2}\right)^2}} + \mathcal{O}(h^{p_g}),$$

where $\frac{\partial \xi_2}{\partial x_1} = \mathcal{O}(h^{-1})$ and $\frac{\partial \xi_2}{\partial x_2} = \mathcal{O}(h^{-1})$ have been used. Therefore, the accuracies of the x_1 and x_2 components of the wall normals are given by

$$n_{x_1} - n_{x_1,h} = \mathcal{O}(h^{p_g}) \quad \text{and, similarly,} \quad n_{x_2} - n_{x_2,h} = \mathcal{O}(h^{p_g}), \tag{47}$$

respectively. Furthermore, since $\tilde{\mathsf{P}}_h = \mathsf{I}_{\xi_1} \otimes \mathsf{I}_4 - \tilde{\boldsymbol{n}}_h \tilde{\boldsymbol{n}}_h^{\mathrm{T}}$ depends directly on the wall normals, the accuracy of $\tilde{\mathsf{P}}_h$ is given by $\tilde{\mathsf{P}}_h = \tilde{\mathsf{P}} + \mathcal{O}(h^{p_g})$. The following term can now be evaluated

$$\begin{aligned} \tilde{\mathsf{P}}_h \mathsf{R}_{\alpha_{\xi_2}} \boldsymbol{u} &= \left\{\tilde{\mathsf{P}} + \mathcal{O}(h^{p_g})\right\} \left\{\boldsymbol{u}_{[3]} + \mathcal{O}(h^{r+1})\right\} \\ &= \tilde{\mathsf{P}}\boldsymbol{u}_{[3]} + \mathcal{O}(h^{r+1}) + \mathcal{O}(h^{p_g}), \end{aligned}$$

since $\tilde{\mathsf{P}} = \mathcal{O}(1)$, $\boldsymbol{u}_{[3]} = \mathcal{O}(1)$, and $\mathcal{O}(h^{p_g})\mathcal{O}(h^{r+1}) = \mathcal{O}(h^{p_g+r+1})$ is a higher order term that can be neglected. Substituting

$$\tilde{\mathsf{P}}_h \mathsf{R}_{\alpha_{\xi_2}} \boldsymbol{u} = \tilde{\mathsf{P}} \boldsymbol{u}_{[3]} + \mathcal{O}(h^{r+1}) + \mathcal{O}(h^{p_g})$$

into $\boldsymbol{f}_{x_m}(\tilde{\mathsf{P}}_h \mathsf{R}_{\alpha_{\xi_2}} \boldsymbol{u})$ and performing a series expansion gives

$$\boldsymbol{f}_{x_m}(\tilde{\mathsf{P}}_h \mathsf{R}_{\alpha_{\xi_2}} \boldsymbol{u}) = \boldsymbol{f}_{x_m}(\tilde{\mathsf{P}} \boldsymbol{u}_{[3]}) + \mathcal{O}(h^{r+1}) + \mathcal{O}(h^{p_g}). \tag{48}$$

Finally, substituting (48) into (46) and using the triangle inequality results in the following expression

$$\left\| \operatorname{diag}(\mathcal{J}_h)^{-1} \operatorname{SAT}^{\boldsymbol{u}}_{\text{Wall}} \right\|_\infty = \mathcal{O}(h^r) + \mathcal{O}(h^{p_g-1}). \tag{49}$$

Since $r \geq p$ by construction, the first term on the right-hand side always satisfies the consistency condition (43). However, the second term on the right-hand side only satisfies the consistency condition (43) when $p_g \geq p+1$, which gives the desired result. □

Theorem 1 explains why superparametric geometry representations are beneficial when solving problems governed by the Euler equations that involve flow tangency boundary conditions. Finally, for the preceding analysis, the normal boundary flux function presented in [22,13] was used. However, similar techniques can be used to show that the numerical boundary flux based on the interior flux function as used by Hartmann and Leicht [14] also satisfies Theorem 1 when used in place of the normal boundary flux function.

5.5 Numerical results

In this section the results of several numerical experiments are presented exploring the properties of the different operators and discretization choices with a particular focus on dual consistency and functional superconvergence. The global H-norm $\|\cdot\|_{\mathsf{H}_g}$ is used to evaluate the different types of solution error measures considered in this section. For example, pressure error is evaluated as follows:

$$\left\|\boldsymbol{p}_{h,g} - \boldsymbol{p}_g\right\|_{\mathsf{H}_g} = \sqrt{(\boldsymbol{p}_{h,g} - \boldsymbol{p}_g)^{\mathrm{T}} \mathsf{H}_g (\boldsymbol{p}_{h,g} - \boldsymbol{p}_g)},$$

where $\boldsymbol{p}_{h,g}$ and $\boldsymbol{p}_g$ are global vectors holding the numerical and exact pressures, respectively, and H_g is the global H-norm matrix. A similar expression is used to evaluate entropy error.

5.5.1 Two-dimensional steady isentropic vortex

The test problem considered in this section is a steady isentropic vortex governed by the Euler equations on a quarter annulus domain. The aims of the studies in this section are as follows: 1) to examine the impact of superparametric geometry representations; 2) to characterize and compare the baseline and modified approaches for approximating the metrics; and 3) to compare the B-spline and Lagrange approaches for constructing high-order grids. The exact density for the steady isentropic vortex is given by

$$\rho(r) = \rho_{\text{in}} \left\{ 1 + \frac{\gamma - 1}{2} M_{\text{in}}^2 \left(1 - \frac{r_{\text{in}}^2}{r^2} \right) \right\}^{1/(\gamma-1)}$$

with the remaining flow quantities being derived via isentropic relations [17]. The solution is characterized by the flow quantities used at the inner radius, which in this case are chosen as $\rho_{\text{in}} = 2$ and $M_{\text{in}} = 0.95$. A perturbation is applied to the grid to prevent grid-dependent error cancellations, by applying the following transformation to a square linear grid prior to applying the polar transformation. The transformation applied to the square linear grid is given by

$$\begin{aligned} x_n &= \xi + \frac{1}{10} \sin(\pi\xi) \sin(\pi\eta), \\ y_n &= \eta + \frac{1}{10} \exp(1 - \eta) \sin\left(\pi\xi - \frac{3}{4} \right) \sin(\pi\eta), \end{aligned}$$

where $[x_n, y_n] \in [0, 1]^2$ are normalized coordinates and $[\xi, \eta] \in [0, 1]^2$. Flow tangency is specified at the inner boundary $r_{\text{in}} = 1$, $\theta \in [0, \pi/2]$ with Dirichlet conditions being weakly imposed via SATs at the remaining boundaries. The outer boundary is given by $r_{\text{out}} = 3$, $\theta \in [0, \pi/2]$. The functional considered is the drag force in the horizontal direction on the inner boundary and in this case can be evaluated exactly as $-1/\gamma$.

Table 9 summarizes the test case parameters considered for this problem and provides an index for the numerical results using Lagrange mappings. Analogous results using B-spline mappings were also produced, and some of those results are shown in Figure 2. For both the Lagrange and B-spline approaches for constructing high-order grids the wall normals are computed directly from either the Lagrange or B-spline mappings at the boundary mortar nodes. For conciseness, in the following tables the data are only provided for the degree two and three operators; however, the figures include results for operators of degree one through four.

Figure 1 gives the convergence of the drag error for the steady vortex problem with the LGL and LG families of operators when using the Lagrange approach for generating the high-order grids as outlined in Section 3. In addition to tabulating the convergence of the drag error, Tables 10, 11, and 12 give the convergence of the entropy and pressure error when using degree p Lagrange mappings with the baseline approach for the metrics, degree $p + 1$

Table 9: Test case matrix and index of numerical results for the steady isentropic vortex problem governed by the Euler equations.

Type of discretization	**Form of equation**	**Metrics**	**Mapping**	p_g	**Table**
Mortar-element	Divergence	Baseline	Lagrange	p	10
Mortar-element	Divergence	Baseline	Lagrange	$p+1$	11
Mortar-element	Divergence	Modified	Lagrange	$p+1$	12

Lagrange mappings with the baseline approach for the metrics, and degree $p+1$ Lagrange mappings with the modified approach for the metrics, respectively. For the LGL operators, there is an improvement in the accuracy of the drag with the degree $p+1$ mappings relative to the degree p mappings due to the accuracy with which the boundary normal in the flow tangency boundary condition can be computed. This agrees with Theorem 1. For the LGL operators, the baseline and modified approaches for the metrics give similar results, with respect to both solution and functional accuracy. With respect to solution accuracy with the LGL operators, only the degree $p = 1$ LGL operators demonstrate a reduction in the error in entropy when going from a degree p geometry representation to a degree $p + 1$ geometry representation, regardless of whether the baseline or modified approach for the metrics is used. In contrast, similar to the observations of Zwanenburg and Nadarajah [35], there is a noticeable reduction in pressure error when going from a degree p to a degree $p + 1$ geometry representation with degree $p = 1$ through $p = 4$ LGL operators, when using either the baseline or modified metrics.

From Figure 1 and Table 10, for the LG operators with degree p mappings, suboptimal functional convergence is obtained due to the accuracy with which the boundary normal can be represented, which is qualitatively similar to the behaviour of the drag error when using the LGL operators with degree p mappings. Referring to Figure 1 and Table 11, increasing the degree of the mappings to $p + 1$ can rectify this issue with the boundary normal; however, using the baseline approach for the metrics with degree $p+1$ mappings leads to significantly reduced functional convergence rates for LG operators since their corresponding extrapolation operators are only degree p accurate. However, from Figure 1 and Table 12, functional superconvergence is recovered for the LG operators with the modified approach for the metrics with degree $p + 1$ mappings. Furthermore, the best case functional convergence rate approaches $2p + 1$ with the LG operators, which is better than the best case functional convergence rate of about $2p$ with the LGL operators.

Referring to Tables 10 and 11, with respect to solution accuracy, the degree $p = 1$ through $p = 4$ LG operators all exhibit reduced entropy error when going from degree p to degree $p + 1$ mappings when using the baseline approach for the metrics. Furthermore, note that the entropy error converges at a rate of at least $p + 1$ when using degree p mappings for the degree $p = 2$ through $p = 4$ LG operators, and that these rates do not increase when using the $p+1$ mappings. Despite this, the absolute value of the entropy error is reduced when

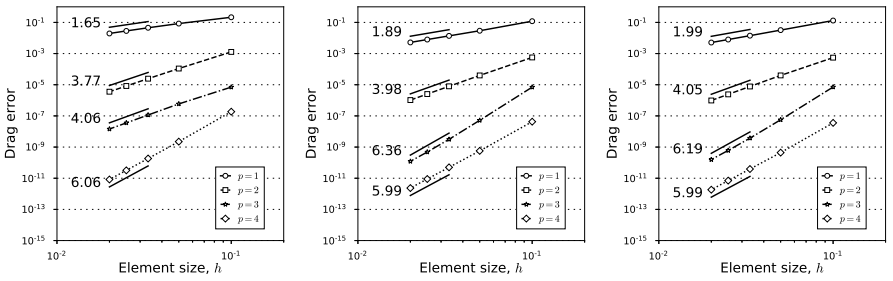

(a) LGL, p, baseline. (b) LGL, $p+1$, baseline. (c) LGL, $p+1$, modified.

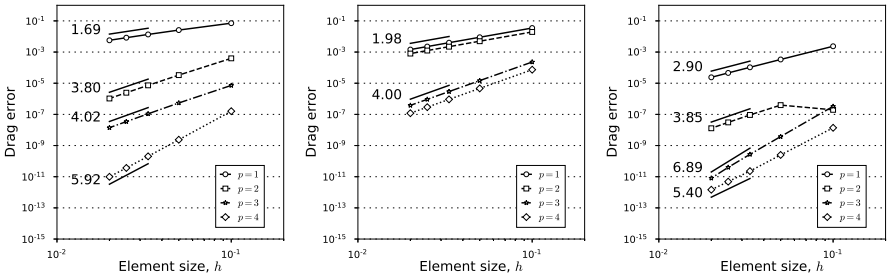

(d) LG, p, baseline. (e) LG, $p+1$, baseline. (f) LG, $p+1$, modified.

Fig. 1: Convergence of drag error for the steady isentropic vortex problem governed by the Euler equations. The caption of each sub plot indicates the operator, degree of mapping, and approach for the metrics, respectively. Lagrange mappings are used.

using degree $p+1$ mappings with the baseline approach for the metrics. Finally, comparing Tables 11 and 12, there is not a notable difference between both the convergence rates and absolute values of the entropy error when using degree $p+1$ mappings with either the baseline or modified metrics for the LG operators. For pressure error with the LG operators, comparing Tables 10 and 11, there is a reduction in pressure error when going from degree p to $p+1$ mappings with baseline metrics; however, in the former case none of the LG operators exhibit $p+1$ convergence rates and in the latter case only the odd-degree LG operators obtain $p+1$ convergence while the even-degree LG operators exhibit p convergence. Finally, comparing Tables 11 and 12, an even greater improvement in pressure error is observed when using the modified metrics with degree $p+1$ mappings with all LG operators considered achieving optimal $p+1$ convergence rates.

The discussion thus far has focused on the results in Figure 1 and Tables 10, 11, and 12, which involve schemes that use the Lagrange approach for constructing high-order grids. Analogous results using the B-spline approach for constructing high-order grids were generated, and a portion of those results are highlighted in Figure 2. Relative to the results with Lagrange mappings, the

Table 10: Numerical results for the mortar-element discretization of the divergence form of the Euler equations when solving the steady isentropic vortex problem using the baseline approach for the metrics with a degree p Lagrange mapping in each element. Table 9 gives the index of numerical results. Convergence rates based on the three finest grids.

		LGL operator error			LG operator error		
p	**Element size**	**Entropy**	**Pressure**	**Drag**	**Entropy**	**Pressure**	**Drag**
2	1.00e−01	6.91e−04	5.66e−03	1.28e−03	2.06e−04	3.97e−03	3.95e−04
	5.00e−02	7.46e−05	1.29e−03	1.10e−04	2.14e−05	8.32e−04	3.32e−05
	3.33e−02	2.16e−05	5.39e−04	2.45e−05	5.69e−06	3.26e−04	7.31e−06
	2.50e−02	9.31e−06	2.85e−04	8.32e−06	2.22e−06	1.66e−04	2.46e−06
	2.00e−02	4.93e−06	1.73e−04	3.57e−06	1.07e−06	9.82e−05	1.05e−06
Convergence rate		2.90	2.22	3.77	3.26	2.35	3.80
3	1.00e−01	4.70e−05	5.92e−04	7.04e−06	2.01e−05	4.11e−04	7.22e−06
	5.00e−02	2.55e−06	7.12e−05	5.88e−07	9.65e−07	4.18e−05	5.40e−07
	3.33e−02	5.26e−07	1.98e−05	1.14e−07	1.62e−07	1.08e−05	1.09e−07
	2.50e−02	1.82e−07	7.84e−06	3.56e−08	4.60e−08	4.14e−06	3.43e−08
	2.00e−02	8.14e−08	3.80e−06	1.44e−08	1.73e−08	1.95e−06	1.40e−08
Convergence rate		3.65	3.23	4.06	4.38	3.36	4.02

Table 11: Numerical results for the mortar-element discretization of the divergence form of the Euler equations when solving the steady isentropic vortex problem using the baseline approach for the metrics with a degree $p + 1$ Lagrange mapping in each element. Table 9 gives the index of numerical results. Convergence rates based on the three finest grids.

		LGL operator error			LG operator error		
p	**Element size**	**Entropy**	**Pressure**	**Drag**	**Entropy**	**Pressure**	**Drag**
2	1.00e−01	3.80e−04	5.67e−03	5.66e−04	9.53e−05	2.23e−03	1.95e−02
	5.00e−02	5.47e−05	7.69e−04	3.95e−05	1.12e−05	5.92e−04	4.97e−03
	3.33e−02	1.80e−05	2.40e−04	7.93e−06	3.24e−06	2.66e−04	2.21e−03
	2.50e−02	8.26e−06	1.05e−04	2.52e−06	1.35e−06	1.50e−04	1.25e−03
	2.00e−02	4.53e−06	5.51e−05	1.04e−06	6.88e−07	9.63e−05	7.98e−04
Convergence rate		2.70	2.88	3.98	3.03	1.99	2.00
3	1.00e−01	3.99e−05	4.36e−04	7.01e−06	5.75e−06	7.23e−05	2.29e−04
	5.00e−02	2.73e−06	2.88e−05	5.20e−08	3.56e−07	4.68e−06	1.47e−05
	3.33e−02	5.90e−07	5.82e−06	3.14e−09	7.02e−08	9.30e−07	2.91e−06
	2.50e−02	2.03e−07	1.87e−06	4.80e−10	2.22e−08	2.95e−07	9.24e−07
	2.00e−02	8.94e−08	7.71e−07	1.22e−10	9.06e−09	1.21e−07	3.79e−07
Convergence rate		3.69	3.96	6.36	4.01	3.99	4.00

results with B-spline mappings are qualitatively similar. The main difference between the two approaches as currently implemented is that the Lagrange approach naturally mimics the stretching of the initial grid within elements while the B-spline approach does not. However, by not mimicking the stretching of the initial grid within elements, the B-spline approach benefits from some error cancellations—potentially associated with the annular geometry and symmetry—that improve its performance relative to the Lagrange approach with respect to solution and functional accuracy. Figure 2 provides an example result comparing the convergence of pressure and drag error with

Table 12: Numerical results for the mortar-element discretization of the divergence form of the Euler equations when solving the steady isentropic vortex problem using the modified approach for the metrics with a degree $p+1$ Lagrange mapping in each element. Table 9 gives the index of numerical results. Convergence rates based on the three finest grids.

		LGL operator error			LG operator error		
p	**Element size**	**Entropy**	**Pressure**	**Drag**	**Entropy**	**Pressure**	**Drag**
2	1.00e−01	4.55e−04	7.01e−03	5.48e−04	8.95e−05	4.50e−04	1.96e−07
	5.00e−02	5.76e−05	9.28e−04	3.96e−05	1.07e−05	5.31e−05	3.93e−07
	3.33e−02	1.85e−05	2.86e−04	7.74e−06	3.12e−06	1.52e−05	9.19e−08
	2.50e−02	8.37e−06	1.23e−04	2.41e−06	1.31e−06	6.28e−06	3.06e−08
	2.00e−02	4.57e−06	6.41e−05	9.77e−07	6.68e−07	3.17e−06	1.29e−08
Convergence rate		2.73	2.92	4.05	3.01	3.07	3.85
3	1.00e−01	4.31e−05	4.55e−04	7.13e−06	5.63e−06	2.19e−05	3.26e−07
	5.00e−02	2.83e−06	2.98e−05	5.64e−08	3.55e−07	1.35e−06	3.76e−09
	3.33e−02	6.03e−07	6.04e−06	3.74e−09	7.01e−08	2.64e−07	2.72e−10
	2.50e−02	2.06e−07	1.94e−06	6.08e−10	2.21e−08	8.24e−08	3.99e−11
	2.00e−02	9.04e−08	8.00e−07	1.59e−10	9.06e−09	3.34e−08	8.06e−12
Convergence rate		3.71	3.96	6.19	4.01	4.04	6.89

LGL operators when using degree $p+1$ Lagrange and B-spline mappings with the modified approach for the metrics. The difference is subtle; however, in general the B-spline approach results in slightly reduced drag and pressure errors compared to the Lagrange approach.

5.5.2 Two-dimensional subsonic channel flow over a Gaussian bump

In this section, subsonic channel flow over a Gaussian bump is considered, governed by the Euler equations. The purpose of this section is to investigate the impact of superparametric geometry representations and to compare the different approaches for the metrics in the context of a somewhat more challenging test case. An efficiency study is also performed, with respect to both total degrees of freedom and core hours. The physical domain for this problem is given by

$$\Omega \coloneqq \left\{ (x_1, x_2) \in [-1.5, 1.5] \times (0, 0.8] \;\middle|\; x_2 > \frac{3}{32} \mathrm{e}^{-25 x_1^2} \right\}.$$

A small perturbation is applied to the grid using the following transformation

$$\begin{aligned} x_n &= \xi + \frac{7}{200} \exp(1-\eta) \sin(\pi\xi) \sin\left(\pi\eta - \frac{7}{4}\right), \\ y_n &= \eta - \frac{7}{200} \sin(\pi\xi) \sin(\pi\eta), \end{aligned}$$

where $[x_n, y_n] \in [0,1]^2$ are normalized coordinates. The boundary conditions are as follows: left boundary—subsonic inflow, right boundary—subsonic outflow, top boundary—symmetry, bottom boundary—flow tangency. The flow tangency and symmetry boundary conditions are enforced by projecting out

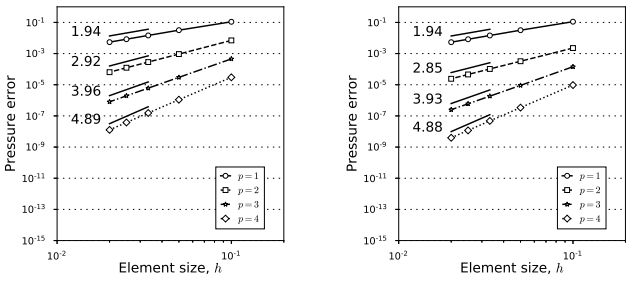

(a) LGL, Lagrange mappings.

(b) LGL, B-spline mappings.

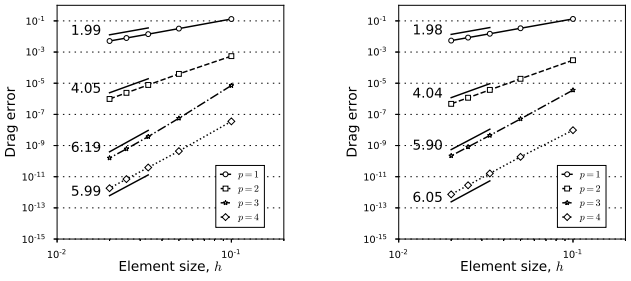

(c) LGL, Lagrange mappings.

(d) LGL, B-spline mappings.

Fig. 2: Convergence of pressure and drag error for the steady isentropic vortex problem governed by the Euler equations. The caption of each sub plot indicates the operator and type of mapping, respectively. Degree $p+1$ mappings with the modified approach for the metrics are used.

the normal component of momentum at the wall as described in Sections 5.1 and 5.3. The subsonic inflow and outflow conditions used are outlined in Appendix B of Fidkowski's Master's thesis [12]. The functional of interest is a weighted lift:

$$\mathcal{I}(\boldsymbol{u}) = \int_{x_1 \in [-1.5,1.5],\, x_2 = \frac{3}{32}\mathrm{e}^{-25x_1^2}} n_{x_2} p(\boldsymbol{u}) \mathrm{e}^{-8x_1^2}\, ds,$$

where the Gaussian weight $\mathrm{e}^{-8x_1^2}$ is used to localize the output around the bump portion of the channel [22]. The flow in the channel is initialized with freestream conditions and driven to a steady state via a parallel Newton-Krylov-Schur algorithm [15, 26].

Table 13 lists the test cases considered for this problem. The grids, metrics, and wall normals are handled in a similar manner to the steady isentropic test case. Figure 3 gives the convergence of the lift error for the steady bump problem with LGL and LG operators when using the Lagrange approach for constructing the high-order grids used in the refinement studies. Tables 14, 15, and 16 give the convergence of the entropy, lift, and drag error when

Table 13: Test case matrix and index of numerical results for the subsonic channel flow over a Gaussian bump problem governed by the Euler equations.

Type of discretization	**Form of equation**	**Metrics**	**Mapping**	p_g	**Table**
Mortar-element	Divergence	Baseline	Lagrange	p	14
Mortar-element	Divergence	Baseline	Lagrange	$p+1$	15
Mortar-element	Divergence	Modified	Lagrange	$p+1$	16

using degree p Lagrange mappings with the baseline approach for the metrics, degree $p+1$ Lagrange mappings with the baseline approach for the metrics, and degree $p+1$ Lagrange mappings with the modified approach for the metrics, respectively. The reference values of lift and drag for this problem are based on a fine grid solution using degree $p = 4$ LG operators with degree $p+1$ Lagrange mappings in each element and using the modified approach for the metrics. The fine grid has 108 elements in the streamwise direction and 36 elements in the normal direction, whereas the finest grid used in the convergence studies has 90 elements in the streamwise direction and 30 elements in the normal direction. For the LGL operators, there is a noticeable benefit in terms of lift error when using degree $p+1$ mappings compared to using degree p mappings due to the increased accuracy with which the boundary normals can be computed in the flow tangency boundary condition. The drag error is already quite accurate with the degree p mapping, potentially due to the symmetry of the problem, and therefore does not benefit nearly as much as the lift error when going from the degree p to the degree $p+1$ mapping. With respect to entropy error, the benefit of using a degree $p+1$ mapping is primarily observed in the context of the degree $p = 1$ operator, consistent with Bassi and Rebay [1]. For the LG operators in Figure 3, the convergence rates of the lift error with the degree p mapping are suboptimal due to the insufficient accuracy of the normals. Likewise, the convergence rates of the lift error with the degree $p+1$ mapping are suboptimal due to the baseline approach for the metrics that involves extrapolating the volume metrics to obtain the surface metrics, which can only be done with degree p accuracy due to the accuracy of the LG extrapolation operators. The results with the degree $p+1$ mappings and modified metrics show that functional superconvergence with respect to lift can be recovered with LG operators and that they can outperform LGL operators in some cases.

Finally, Figure 4 gives the efficiency of the various best-case schemes with respect to total degrees of freedom and core hours, respectively, where

$$\text{core hours} = (\text{number of cores}) \times (\text{wall-clock time in hours})\,.$$

Results with degree one through three CSBP operators under traditional refinement are included for comparison. The results with the LGL/LG and CSBP schemes were obtained using 12 Intel cores each. Furthermore, for all cases the system is solved to relative and absolute residual norm tolerances of 10^{-12}. For the CSBP schemes, the wall normals are approximated by constructing

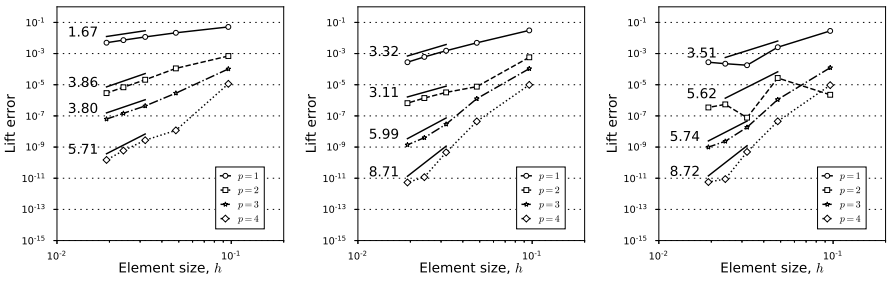

(a) LGL, p, baseline. (b) LGL, $p+1$, baseline. (c) LGL, $p+1$, modified.

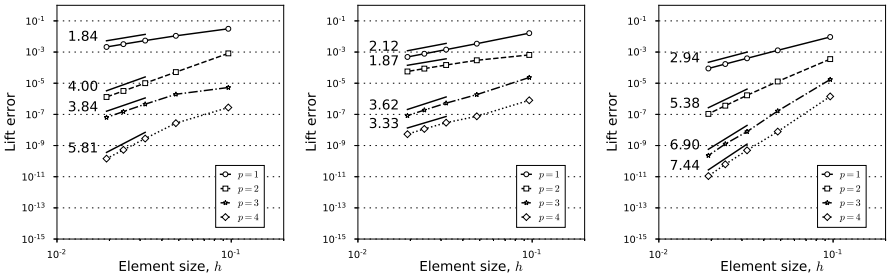

(d) LG, p, baseline. (e) LG, $p+1$, baseline. (f) LG, $p+1$, modified.

Fig. 3: Convergence of lift error for the subsonic channel flow over a Gaussian bump problem governed by the Euler equations. The caption of each sub plot indicates the operator, degree of mapping, and approach for the metrics, respectively. Lagrange mappings are used.

degree $p+1$ one-sided stencils at the boundaries. High-order grids for the CSBP schemes considered are constructed directly using the exact analytical mapping and the alternative approach for computing the wall normals summarized above is used along with the baseline approach for the metrics. Referring to Figure 4, in terms of total degrees of freedom, the purely element-type schemes are generally more accurate. In contrast, the CSBP schemes with traditional refinement can be more efficient with respect to core hours due to the decreased number of SATs and increased sparsity relative to the purely element-type schemes. Finally, the competitiveness of the CSBP schemes in the current context is partially due to the smoothness of the grids considered. For more distorted or highly-stretched grids, it is expected that the efficiency of the LGL/LG schemes would improve relative to the CSBP schemes.

6 Conclusions

High-order tensor-product generalized SBP discretizations have been investigated and conditions for obtaining accurate solutions and functionals for CFD

Table 14: Numerical results for the mortar-element discretization of the divergence form of the Euler equations when solving the subsonic channel flow over a Gaussian bump problem using the baseline approach for the metrics with a degree p Lagrange mapping in each element. Table 13 gives the index of numerical results. Convergence rates based on the three finest grids.

		LGL operator error			LG operator error		
p	**Element size**	**Entropy**	**Lift**	**Drag**	**Entropy**	**Lift**	**Drag**
2	9.62e−02	6.52e−04	6.96e−04	2.48e−04	3.00e−04	8.23e−04	3.74e−04
	4.81e−02	9.25e−05	1.12e−04	4.12e−05	3.69e−05	5.18e−05	2.09e−05
	3.21e−02	2.53e−05	2.09e−05	6.37e−06	9.59e−06	1.01e−05	3.90e−06
	2.41e−02	1.19e−05	6.89e−06	2.01e−06	3.62e−06	3.19e−06	1.21e−06
	1.92e−02	7.31e−06	2.91e−06	8.18e−07	1.70e−06	1.31e−06	4.90e−07
Convergence rate		2.43	3.86	4.02	3.39	4.00	4.06
3	9.62e−02	1.60e−04	1.03e−04	6.02e−05	6.04e−05	5.30e−06	1.30e−05
	4.81e−02	9.15e−06	2.88e−06	7.33e−07	2.52e−06	1.95e−06	2.86e−07
	3.21e−02	2.55e−06	4.36e−07	4.63e−09	3.55e−07	4.52e−07	2.79e−08
	2.41e−02	1.10e−06	1.46e−07	4.24e−10	1.01e−07	1.52e−07	4.65e−09
	1.92e−02	5.50e−07	6.25e−08	3.42e−10	3.63e−08	6.37e−08	1.11e−09
Convergence rate		3.00	3.80	5.10	4.46	3.84	6.31

Table 15: Numerical results for the mortar-element discretization of the divergence form of the Euler equations when solving the subsonic channel flow over a Gaussian bump problem using the baseline approach for the metrics with a degree $p + 1$ Lagrange mapping in each element. Table 13 gives the index of numerical results. Convergence rates based on the three finest grids.

		LGL operator error			LG operator error		
p	**Element size**	**Entropy**	**Lift**	**Drag**	**Entropy**	**Lift**	**Drag**
2	9.62e−02	7.18e−04	5.78e−04	4.98e−04	1.93e−04	6.53e−04	1.38e−03
	4.81e−02	8.95e−05	7.54e−06	6.44e−06	2.78e−05	2.97e−04	1.66e−04
	3.21e−02	2.56e−05	3.23e−06	2.04e−06	7.47e−06	1.48e−04	5.00e−05
	2.41e−02	1.22e−05	1.40e−06	9.04e−07	2.85e−06	8.66e−05	2.21e−05
	1.92e−02	7.50e−06	6.59e−07	4.42e−07	1.34e−06	5.67e−05	1.20e−05
Convergence rate		2.41	3.11	2.99	3.36	1.87	2.80
3	9.62e−02	1.68e−04	1.08e−04	5.85e−05	5.64e−05	2.33e−05	1.37e−05
	4.81e−02	9.93e−06	1.28e−06	1.18e−06	2.42e−06	1.86e−06	6.60e−07
	3.21e−02	2.62e−06	2.94e−08	4.01e−08	3.45e−07	5.26e−07	8.75e−08
	2.41e−02	1.12e−06	3.99e−09	8.39e−09	9.81e−08	1.89e−07	1.92e−08
	1.92e−02	5.55e−07	1.38e−09	2.44e−09	3.55e−08	8.28e−08	5.80e−09
Convergence rate		3.04	5.99	5.48	4.45	3.62	5.31

problems of increasing practical complexity have been delineated. In Section 3, two procedures for constructing high-order grids were presented based on Lagrange polynomials and B-splines. The requirements for achieving functional superconvergence with generalized SBP discretizations of the linear convection (Section 4) and Euler (Section 5) equations were outlined. The main features of a discretization affecting functional superconvergence include the representation of the geometry, the approximation of the metrics, and the approximation of the normals appearing in the flow tangency boundary condition. Work remains to determine the analogous requirements for obtaining accurate

Table 16: Numerical results for the mortar-element discretization of the divergence form of the Euler equations when solving the subsonic channel flow over a Gaussian bump problem using the modified approach for the metrics with a degree $p+1$ Lagrange mapping in each element. Table 13 gives the index of numerical results. Lift and drag convergence rates for the degree $p=2$ operators are based on the three middle grids. Convergence rates for entropy error and the degree $p=3$ operators are based on the three finest grids.

		LGL operator error			**LG operator error**		
p	**Element size**	**Entropy**	**Lift**	**Drag**	**Entropy**	**Lift**	**Drag**
2	9.62e−02	8.46e−04	2.27e−06	2.22e−05	2.06e−04	3.53e−04	2.14e−04
	4.81e−02	1.04e−04	2.70e−05	2.06e−05	2.94e−05	1.29e−05	1.07e−05
	3.21e−02	2.89e−05	7.71e−08	1.31e−07	7.97e−06	1.68e−06	1.52e−06
	2.41e−02	1.31e−05	5.48e−07	3.56e−07	3.06e−06	3.62e−07	3.72e−07
	1.92e−02	7.83e−06	3.49e−07	2.55e−07	1.45e−06	1.07e−07	1.25e−07
Convergence rate		2.98	5.62	5.85	3.27	5.16	4.85
3	9.62e−02	1.61e−04	1.24e−04	7.36e−05	5.36e−05	1.73e−05	1.34e−05
	4.81e−02	1.00e−05	1.12e−06	1.08e−06	2.44e−06	1.65e−07	1.12e−07
	3.21e−02	2.62e−06	1.86e−08	3.38e−08	3.58e−07	7.83e−09	7.71e−09
	2.41e−02	1.11e−06	2.35e−09	7.59e−09	1.02e−07	1.26e−09	1.24e−09
	1.92e−02	5.51e−07	9.91e−10	2.28e−09	3.69e−08	2.30e−10	2.59e−10
Convergence rate		3.05	5.74	5.28	4.45	6.90	6.64

solutions and functionals for more complex problems based on large eddy simulations and those involving the Reynolds-averaged Navier-Stokes equations.

Acknowledgements A portion of the plots appearing in this paper were created using Matplotlib [19].

References

1. Bassi, F., Rebay, S.: High-order accurate discontinuous finite element solution of the 2D Euler equations. Journal of Computational Physics **138**, 251–285 (1997)
2. Boom, P.D.: High-order implicit time-marching methods for unsteady fluid flow simulation. Ph.D. thesis, University of Toronto (2015)
3. Boom, P.D., Zingg, D.W.: High-order implicit time-marching methods based on generalized summation-by-parts operators. SIAM Journal on Scientific Computing **37**(6), A2682–A2709 (2015)
4. Cockburn, B., Wang, Z.: Adjoint-based, superconvergent Galerkin approximations of linear functionals. Journal of Scientific Computing **73**(2-3), 644–666 (2017)
5. Craig Penner, D.A., Zingg, D.W.: Superconvergent functional estimates from tensor-product generalized summation-by-parts discretizations in curvilinear coordinates. Journal of Scientific Computing **82**(41) (2020)
6. Crean, J., Hicken, J.E., Del Rey Fernández, D.C., Zingg, D.W., Carpenter, M.H.: Entropy-stable summation-by-parts discretization of the Euler equations on general curved elements. Journal of Computational Physics **356**, 410–438 (2018)
7. Del Rey Fernández, D.C., Boom, P.D., Carpenter, M.H., Zingg, D.W.: Extension of tensor-product generalized and dense-norm summation-by-parts operators to curvilinear coordinates. Journal of Scientific Computing **80**(3), 1957–1996 (2019)
8. Del Rey Fernández, D.C., Boom, P.D., Zingg, D.W.: A generalized framework for nodal first derivative summation-by-parts operators. Journal of Computational Physics **266**, 214–239 (2014)

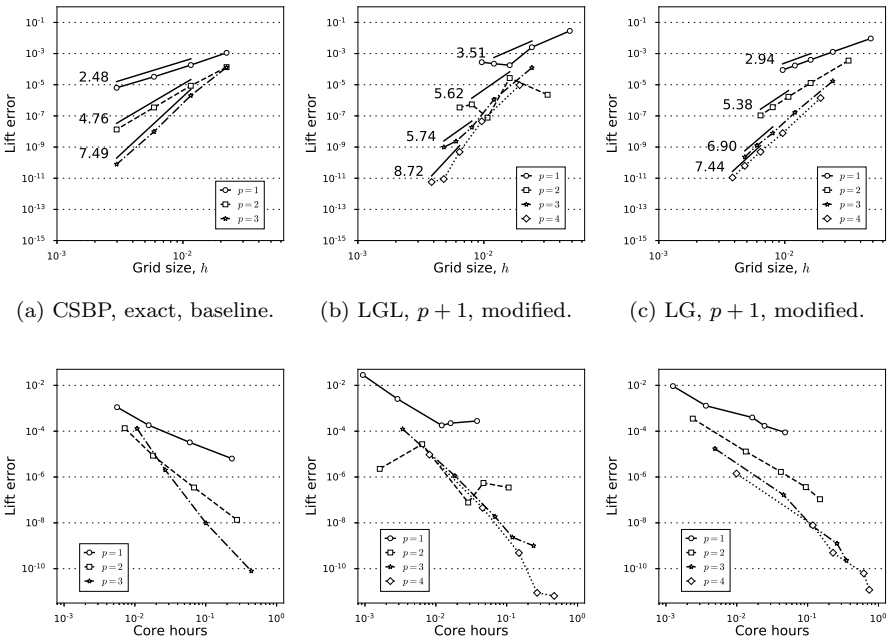

(a) CSBP, exact, baseline. (b) LGL, $p+1$, modified. (c) LG, $p+1$, modified.

(d) CSBP, exact, baseline. (e) LGL, $p+1$, modified. (f) LG, $p+1$, modified.

Fig. 4: Convergence of lift error as a function of grid size based on the total number of grid nodes and core hours for the subsonic channel flow over a Gaussian bump problem governed by the Euler equations. The caption of each sub plot indicates the operator, degree of mapping, and approach for the metrics, respectively. Lagrange mappings are used for the LGL and LG schemes.

9. Del Rey Fernández, D.C., Hicken, J.E., Zingg, D.W.: Review of summation-by-parts operators with simultaneous approximation terms for the numerical solution of partial differential equations. Computers & Fluids **95**, 171–196 (2014)
10. Del Rey Fernández, D.C., Hicken, J.E., Zingg, D.W.: Simultaneous approximation terms for multi-dimensional summation-by-parts operators. Journal of Scientific Computing **75**(1), 83–110 (2018)
11. Deng, X., Min, Y., Mao, M., Liu, H., Tu, G., Zhang, H.: Further studies on geometric conservation law and applications to high-order finite difference schemes with stationary grids. Journal of Computational Physics **239**, 90–111 (2013)
12. Fidkowski, K.J.: A high-order discontinuous galerkin multigrid solver for aerodynamic applications. SM thesis, Massachusetts Institute of Technology (2004)
13. Hartmann, R.: Adjoint consistency analysis of discontinuous Galerkin discretizations. SIAM Journal on Numerical Analysis **45**(6), 2671–2696 (2007)
14. Hartmann, R., Leicht, T.: Generalized adjoint consistent treatment of wall boundary conditions for compressible flows. Journal of Computational Physics **300**, 754–778 (2015)
15. Hicken, J.E., Zingg, D.W.: Parallel Newton-Krylov solver for the Euler equations discretized using simultaneous approximation terms. AIAA Journal **46**(11), 2773–2786 (2008)

16. Hicken, J.E., Zingg, D.W.: Aerodynamic optimization algorithm with integrated geometry parameterization and mesh movement. AIAA Journal **48**(2), 400–413 (2010)
17. Hicken, J.E., Zingg, D.W.: Superconvergent functional estimates from summation-by-parts finite-difference discretizations. SIAM Journal on Scientific Computing **33**(2), 893–922 (2011)
18. Hicken, J.E., Zingg, D.W.: Dual consistency and functional accuracy: a finite-difference perspective. Journal of Computational Physics **256**, 161–182 (2014)
19. Hunter, J.D.: Matplotlib: A 2D graphics environment. Computing in Science & Engineering **9**(3), 90–95 (2007)
20. Krivodonova, L., Berger, M.: High-order accurate implementation of solid wall boundary conditions in curved geometries. Journal of Computational Physics **211**(2), 492–512 (2006)
21. Loken, C., Gruner, D., Groer, L., Peltier, R., Bunn, N., Craig, M., Henriques, T., Dempsey, J., Yu, C.H., Chen, J., Dursi, L.J., Chong, J., Northrup, S., Pinto, J., Knecht, N., Zon, R.V.: SciNet: Lessons learned from building a power-efficient top-20 system and data centre. Journal of Physics: Conference Series **256**, 012026 (2010)
22. Lu, J.C.C.: An a posteriori error control framework for adaptive precision optimization using discontinuous Galerkin finite element method. Ph.D. thesis, Massachusetts Institute of Technology (2005)
23. Navah, F.: Development, verification and validation of high-order methods for the simulation of turbulence. Ph.D. thesis, McGill University (2018)
24. Navah, F., Nadarajah, S.: On the verification of CFD solvers of all orders of accuracy on curved wall-bounded domains and for realistic RANS flows. Computers & Fluids **205** (2020)
25. Nolasco, I.R., Dalcin, L., Del Rey Fernández, D.C., Zampini, S., Parsani, M.: Optimized geometrical metrics satisfying free-stream preservation. Computers & Fluids **207** (2020)
26. Osusky, M., Zingg, D.W.: Parallel Newton–Krylov–Schur flow solver for the Navier–Stokes equations. AIAA Journal **51**(12), 2833–2851 (2013)
27. Pierce, N.A., Giles, M.B.: Adjoint recovery of superconvergent functionals from PDE approximations. SIAM Review **42**(2), 247–264 (2000)
28. Pulliam, T.H., Zingg, D.W.: Fundamental Algorithms in Computational Fluid Dynamics. Scientific Computation. Springer International Publishing (2014)
29. Svärd, M., Nordström, J.: Review of summation-by-parts schemes for initial-boundary-value problems. Journal of Computational Physics **268**, 17–38 (2014)
30. Thomas, P.D., Lombard, C.K.: Geometric conservation law and its application to flow computations on moving grids. AIAA Journal **17**(10), 1030–1037 (1979)
31. van der Vegt, J.J.W., van der Ven, H.: Slip flow boundary conditions in discontinuous Galerkin discretizations of the Euler equations of gas dynamics. Tech. Rep. NLR-TP-2002-300, National Aerospace Laboratory NLR (2002)
32. Vinokur, M., Yee, H.: Extension of efficient low dissipation high order schemes for 3-D curvilinear moving grids. In: Frontiers of Computational Fluid Dynamics 2002, pp. 129–164 (2001)
33. Worku, Z.A., Zingg, D.W.: Simultaneous approximation terms and functional accuracy for diffusion problems discretized with multidimensional summation-by-parts operators. Journal of Computational Physics **445** (2021)
34. Yan, J., Crean, J., Hicken, J.E.: Interior penalties for summation-by-parts discretizations of linear second-order differential equations. Journal of Scientific Computing **75**(3), 1385–1414 (2018)
35. Zwanenburg, P., Nadarajah, S.: On the necessity of superparametric geometry representation for discontinuous Galerkin methods on domains with curved boundaries. In: 23rd AIAA Computational Fluid Dynamics Conference (2017)

Statements and declarations

Funding

This work was supported by the Natural Sciences and Engineering Research Council of Canada, the Government of Ontario, and the University of Toronto. A portion of the computations were performed on the Niagara supercomputer at the SciNet HPC Consortium [21]. SciNet is funded by: the Canada Foundation for Innovation; the Government of Ontario; Ontario Research Fund - Research Excellence; and the University of Toronto.

Competing interests

The authors have no competing interests to declare.

Author contributions

David A. Craig Penner: Conceptualization, Methodology, Software, Writing – original draft; David W. Zingg: Conceptualization, Methodology, Supervision, Writing – review & editing.

Data availability

Not applicable.